

Molecular resonance identification in complex absorbing potentials via integrated quantum computing and high-throughput computing

Jingcheng Dai,^{†,a} Atharva Vidwans,^{†,a,b} Eric H. Wan,^{c,d} Alexander X. Miller, and
Micheline B. Soley^{a,b,e*}

^a*Department of Chemistry, University of Wisconsin-Madison, 1101 University Avenue,
Madison, WI 53706, USA*

^b*Department of Physics, University of Wisconsin-Madison, 1150 University Avenue,
Madison, WI 53706, USA*

^c*Department of Mathematics, University of Wisconsin-Madison, 480 Lincoln Drive,
Madison, WI 53706, USA*

^d*Department of Computer Sciences, University of Wisconsin-Madison, 1210 West Dayton
Street, Madison, WI 53706, USA*

^e*Data Science Institute, University of Wisconsin-Madison, 447 Lorch Street, Madison, WI
53706, USA*

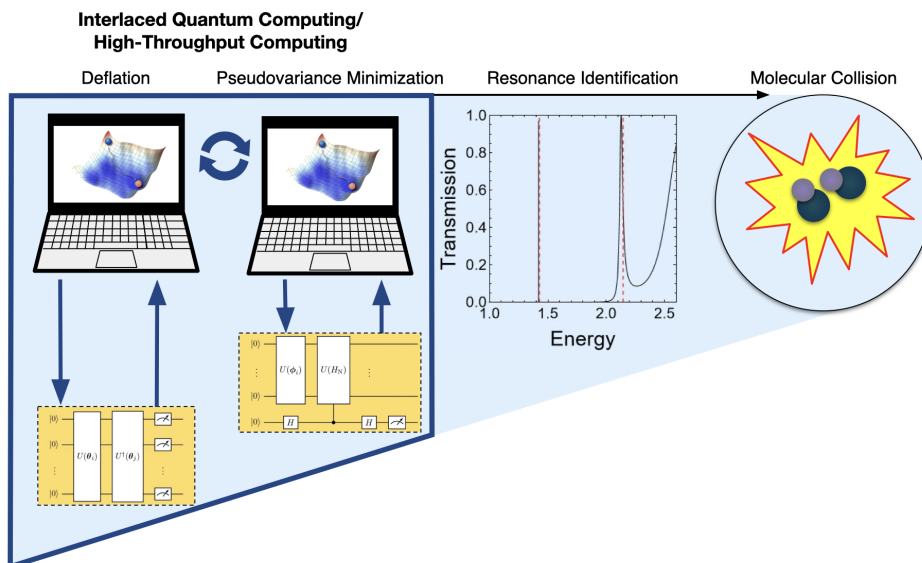
[†]*These authors contributed equally to this work.*

**Corresponding Author*

E-mail: msoley@wisc.edu

Abstract

Recent advancements in quantum algorithms have reached a state where we can consider how to capitalize on quantum and classical computational resources to accelerate molecular resonance state identification. Here we identify molecular resonances with a method that combines quantum computing with classical high-throughput computing (HTC). This algorithm, which we term qDRIVE (the quantum deflation resonance identification variational eigensolver) exploits the complex absorbing potential formalism to distill the problem of molecular resonance identification into a network of hybrid quantum-classical variational quantum eigensolver tasks, and harnesses HTC resources to execute these interconnected but independent tasks both asynchronously and in parallel, a strategy that minimizes wall time to completion. We show qDRIVE successfully identifies resonance energies and wavefunctions in simulated quantum processors with current and planned specifications, which bodes well for qDRIVE's ultimate application in disciplines ranging from photocatalysis to quantum control and places a spotlight on the potential offered by integrated heterogeneous quantum computing/HTC approaches in computational chemistry.



Introduction

To date, much of the focus on quantum algorithms in chemistry has been placed on identification of the ground state and excited states of Hermitian Hamiltonians.¹⁻¹⁷ However, an emerging interest lies in open quantum systems, both to simulate realistic chemical systems in contact with surrounding environments¹⁸ and to characterize physical systems — including molecular qubits — to use as the basis of novel quantum computing architectures.¹⁹ The newfound interest in open quantum systems has led to the development of quantum algorithms to identify eigenstates of associated non-Hermitian Hamiltonians,²⁰⁻²⁹ including left- and right-eigenvectors associated with parity-time reversal (\mathcal{PT}) symmetry breaking at exceptional points^{28,29} and resonances (purely outgoing eigenstates) associated with decay processes.^{21,24,27,30}

Quantum algorithms for resonance identification are of particular relevance in today’s computational chemistry since resonances are ubiquitous for the description of molecular breakup processes in chemistry ranging from ultracold collision complex decay³¹ to plasmonic photocatalysis.³² Recent predictions also suggest molecular resonances could play a key role in the ongoing second quantum revolution with impacts to both quantum information processing³³ and quantum control.³⁴ Many classical methods to identify resonances exist, such as approaches based on complex absorbing potentials (CAPs),³⁵⁻³⁹ complex scaling,^{40,41} Feshbach projection,⁴²⁻⁴⁴ the stabilization method,⁴⁵⁻⁴⁷ analytic continuation in the coupling constant,^{48,49} and R-matrix theory⁵⁰. However, contemporary methods for molecular resonance identification often struggle with exacting parameter dependence and/or sizeable basis sets.³² This begets the question: how can we harness available computational resources — both quantum and classical — to facilitate and accelerate molecular resonance identification?

Current quantum algorithms that address this question tend to fall into two categories.¹ The first category comprises algorithms based on quantum phase estimation. This category

¹Note an outlier, the Quantum Annealer Eigensolver,²⁴ which is specifically designed for use on quantum annealing (e.g., D-Wave) systems.⁵¹

can be considered to include algorithms such as measurement-based quantum phase estimation,²⁰ iterative phase estimation,²¹ generalizations of quantum phase estimation,^{22,23,25} the iterative Harrow-Hassidim-Lloyd approach,⁵² and the direct measurement method.^{27,53,54} Since quantum phase estimation tends to call for a high circuit depth (gate count), algorithms in this category are often best suited for fault-tolerant quantum computers still under development. The second category comprises algorithms that adapt the variational quantum eigensolver (VQE)^{3,55-58} to non-Hermitian systems. This category can be considered to include algorithms such as the Variational Quantum Universal Eigensolver²⁶ and Xie-Xue-Zhang method²⁸⁻³⁰. Since these algorithms rely on a VQE-like approach, algorithms in this category typically require lower circuit depths than algorithms based on quantum phase estimation, and thus are more naturally suited to existing noisy intermediate scale quantum (NISQ) computers. The adaptation of VQE to non-Hermitian systems entails an added computational cost related to preparation of the Ansatz (trial or guess state); for example, the Variational Quantum Universal Eigensolver requires preliminary precise training²⁶ and the Xie-Xue-Zhang method requires both parametrization of and scans over the eigenenergy.²⁸

In this study, we facilitate molecular resonance identification by combining the complex absorbing potential (CAP) formalism with an interlaced quantum computing/parallel asynchronous high-throughput computing (HTC) approach that we term qDRIVE (the quantum deflation resonance identification variational eigensolver).

We recognize that the construction of CAPs enables us to prepare a physically motivated Ansatz without precise training or energy parametrization as follows: In the CAP formalism,^{32,35-39,59,60} resonances are identified by appending to the original potential of interest V_0 a negative imaginary potential at the outer reaches of the simulation window iV_{CAP} to impose purely outgoing boundary conditions. The CAP formalism thus entails two Hamiltonians: a Hermitian Hamiltonian H_{H} comprised of the system’s physical kinetic and potential energy and an artificial non-Hermitian Hamiltonian that is only made non-Hermitian by the imposition of boundary conditions with a CAP H_{N} . Since the two Hamiltonians differ only

at the extremities of the simulation window, their eigenstates are, in many systems, likely to be similar in the internal region. Therefore, an effective initial guess for an eigenstate of the non-Hermitian Hamiltonian is often the corresponding eigenstate of the Hermitian Hamiltonian. qDRIVE uses this strategy to prepare the initial Ansatz for the non-Hermitian Hamiltonian resonance as the corresponding eigenstate of the Hermitian Hamiltonian. This identification of the required Hermitian Hamiltonian eigenstates is a straightforward task on quantum computers with VQE^{3,55-58} and its excited-state analog, variational quantum deflation (VQD).¹⁰

Importantly, CAP-based qDRIVE provides the means to sidestep many of the complexities involved in non-Hermitian quantum mechanics. Specifically, in Hermitian quantum mechanics, wavefunctions are decomposed in terms of the complete set of eigenfunctions of a Hermitian operator, where orthogonality is determined according to the standard scalar product $\langle \psi | \phi \rangle = \int dx \psi^*(x) \phi(x)$. In non-Hermitian quantum mechanics, decomposition of wavefunctions instead requires the c-product given by $(\psi | \phi) = \int dx \psi(x) \phi(x)$.^{61,62} Here a significant complication arises – eigenvalues of a non-Hermitian operator can coalesce, as often occurs in parity-time-reversal-symmetric (\mathcal{PT} -symmetric) systems⁶³⁻⁶⁵ and in complex scaling at the complex rotation angle where continuum and resonance solutions meet.⁶⁶ In this case, eigenvalues become defective and exceptional points appear; and eigenfunctions themselves coalesce such that the spectrum becomes incomplete or defective. Simulation methods must then contend with self-orthogonality, in which the c-product becomes zero, and an accompanying lack of biorthogonal completeness. Such a situation typically calls for special adaptations such as the inclusion of functions beyond true eigenfunctions in order to ensure closure relations hold.⁶⁷

CAP-based resonance identification in qDRIVE allays these concerns at two levels: Firstly, at the algorithmic level, by construction, qDRIVE never calls for calculation of the c-product, only the standard scalar product, for which these problems do not occur. Secondly, at the NISQ computing level, inherent quantum processor error is expected to break apart de-

generacies. It is well known that an infinitesimal perturbation is sufficient to destroy an exceptional point: for example, round-off error is sufficient to avoid a zero c-product in finite-element approaches.^{66,67} By definition, NISQ computers similarly involve a significant (typically larger) degree of error, both in terms of thermal and gate noise and in terms of limitations on the gate count that lead to finite Ansatz expressibility. Just as round-off error pushes systems away from the exceptional point on classical processors, NISQ systems' error is similarly expected to drive systems away from exact exceptional points to allow for the restoration of biorthogonal completeness.

Today, there is active discussion on how to employ high-performance computing (HPC) resources to accelerate quantum information processing tasks.⁶⁸⁻⁷¹ Traditionally, such HPC approaches accelerate computation by running blocks of jobs in parallel, often with tight communication between jobs. However, where HPC resources are limited, such an approach can require large wait times until a block of a suitable size becomes available. In contrast, HTC follows a vulture's approach that scavenges individual available computational cores as they become available to run jobs — still in parallel, but now asynchronously as resources allow.⁷²⁻⁷⁸ This HTC approach maximizes throughput of computational tasks performed by the supercomputer over time, an important tack where supercomputing resources are scarce. qDRIVE consists of a network of interconnected but independently executable jobs. This network can be readily expressed as a directed acyclic graph, which can be implemented on HTC resources with HTCondor DAGMan (the HTCondor directed acyclic graph manager).⁷²⁻⁷⁸

Typically, HTCondor DAGMan uses fall into three main categories based on the instructed order of task operations: (1) sequential DAGs, in which task A is completed prior to task B, task B prior to task C, and so on; (2) split-and-recombine DAGs, in which a task begets many tasks that feed into a single shared task; and (3) collection DAGs, in which there is no ordering of tasks to be completed.⁷⁹ qDRIVE uses a DAG that falls outside these categories. This DAG can be described rigorously as an arborescence in which each parent

node leads to a child node of the same connectivity and a child node with no children. Such an interlaced DAG hybridizes the cascading nature of a sequential DAG with the spawning ability of a split-and-recombine DAG. In addition, the DAG itself is executed in separate batch runs, such that the DAG also shares the embarrassingly parallel characteristic nature of a collection DAG. This innovative hybrid DAG approach accelerates completion of all of qDRIVE’s interdependent Hermitian and non-Hermitian Hamiltonian stages by closely mirroring qDRIVE’s algorithmic structure and the execution of tasks with the DAGMan metascheduler.

To the knowledge of the authors, the framework introduced in qDRIVE is the only framework to harness HTC resources in quantum computing for chemical applications to date in the literature. The only known use of comparable high-throughput computing systems in quantum computing is the use of HTCondor to simulate quantum computers classically,⁸⁰ which constitutes a distinct goal from the acceleration of hybrid quantum-classical algorithms that may employ real quantum computers as put forward here. The HTC framework introduced in qDRIVE is therefore expected to be of unique benefit to researchers seeking to accelerate completion of hybrid quantum-classical algorithm jobs, as well as to those who have access to publicly available HTC resources such as the Open Science Grid but who may have only limited access to more widely known HPC resources.^{81,82}

In proof-of-concept experiments using a variety of quantum simulators, we show qDRIVE identifies the bound and resonance states of a long-established benchmark model of molecular predissociation^{53,62} (i) in the zero-noise limit and (ii) on NISQ systems in conjunction with the practical error mitigation techniques^{83,84} of readout matrix inversion⁸⁵⁻⁸⁷ and hybrid linear-exponential zero-noise extrapolation (ZNE)^{83,88-91}. For the same system, we also show qDRIVE fares well (iii) in far-term environments, modeled by the anticipated gate errors and qubit longevities of quantum processors on the horizon. These successes show that qDRIVE can be used to identify molecular resonance states capitalizing on a joint quantum computing and HTC heterogenous computing approach.

Methods

qDRIVE Algorithmic Framework

As the basis of a quantum algorithm for molecular resonance identification in the complex absorbing potential (CAP) formalism,^{32,35-39,59,60} we consider the class of Siegert pseudostates defined as the purely outgoing eigenstates of a non-Hermitian Hamiltonian H_N given by the sum of (i) the Hermitian Hamiltonian H_H corresponding to the purely real potential V_0 of interest and (ii) a complex absorbing potential (CAP) V_{CAP}

$$H_N = H_H + iV_{CAP} \quad (1)$$

where V_{CAP} is purely a real potential that is zero in the internal region of physical interest and negative near the simulation boundary in order to impose purely outgoing boundary conditions. Eigenstates of the resulting non-Hermitian Hamiltonian are complex in energy $E = E_r - iE_i$ with an imaginary part that corresponds to the resonance decay rate $E_i = \Gamma/2$ and lifetime $\tau = \Gamma^{-1}$. Note practical identification of physical Siegert states $H_N\psi = E\psi$ further requires omission of spurious resonance states that correspond to artifacts native to the CAP method (namely, nonresonant, diverging, and indifferent states, see ref. 92).

To characterize resonances in this CAP formalism, we consider the purely nonnegative metric for a Hamiltonian H_O of

$$\sigma_{\text{pseudo}}^2 = \langle H_O^\dagger H_O \rangle - \langle H_O^\dagger \rangle \langle H_O \rangle, \quad (2)$$

where the subscript $O = \{H, N\}$ denotes the Hermiticity or non-Hermiticity of the Hamiltonian, respectively, and where we refer to the metric as the pseudovariance to distinguish the metric from the standard, simplified variance formula for Hermitian Hamiltonians $O = H$ used in standard Variance VQE⁹³ and related variance-based quantum algorithms for excited state determination such as the contracted quantum eigensolver (CQE),^{15,94} VQE-X,⁹⁵

CoVaR,⁹⁶ and excited-state variance VQE,^{97,98} namely,

$$\sigma^2 = \langle H_O^2 \rangle - \langle H_O \rangle^2, \quad (3)$$

for $O = H$, which yields a nonordered field if applied to generic non-Hermitian matrices $O = N$. This pseudovariance metric assumes the same form as the squared-residual cost function used in variance VQE to identify right eigenvectors of non-Hermitian Hamiltonians²⁸ with the key exception that the pseudovariance analytically eliminates dependence on an energy parameter. Note that, since the pseudovariance obviates the need for an energy parameter, use of the pseudovariance circumvents the parameter scan required by prior non-Hermitian Variance VQE approaches.²⁸⁻³⁰ Furthermore, since the CAP-based Hamiltonian H_N Eq. (1) is given by the sum of a Hermitian Hamiltonian H_H and a purely imaginary term iV_{CAP} , its expectation value $\langle H_N \rangle$ follows directly from the expectation values of two Hermitian operators, namely, $\langle H_N \rangle = \langle H_H \rangle + i \langle V_{CAP} \rangle$. This decomposition allows the expectation value of the energy of a resonance to be computed using only the scalar product⁹² $\langle \psi | \phi \rangle = \int dx \psi^*(x) \phi(x)$, without recourse to the standard c-product used for generic non-Hermitian systems ($\psi | \phi \rangle = \int dx \psi(x) \phi(x)$).^{61,62} Similar arguments hold for the remaining terms of the pseudovariance $\langle H_N^\dagger \rangle$ and $\langle H_N^\dagger H_N \rangle$ such that (i) the pseudovariance may be computed using only the standard scalar product and thereby its associated quantum circuits^{3,58} without recourse to twin pairs of left- and right-eigenvector Ansatz parameters^{28,29} and (ii) the pseudovariance can be shown to be purely nonnegative and to feature global minima of zero only for eigenstates, *i.e.*,

$$\sigma_{\text{pseudo}}^2 \geq 0 \quad (4)$$

where $\sigma_{\text{pseudo}}^2 = 0$ for states ψ that satisfy $H_N \psi = E \psi$.

These characteristics of the pseudovariance, combined with the aforementioned close relationship between H_N and H_H in the CAP formalism, enable the identification of N

eigenstates of H_N according to the scheme depicted in Fig. 1 and outlined below:

1. Consider a parametrized Ansatz wavefunction $\psi(\theta)$ subject to the CAP-based Hamiltonian $H_N = H_H + iV_{\text{CAP}}$ and initialize $i = 1$ and a set of random parameters $\{\theta_i\}$.
2. For the Hermitian Hamiltonian H_H , determine the Ansatz parameters θ_i that correspond to the i^{th} eigenstate via optimization of the objective function

$$\langle \psi(\theta_i) | H_H | \psi(\theta_i) \rangle + c \sum_{j < i} |\langle \psi(\theta_i) | \psi(\theta_j) \rangle|^2 \quad (5)$$

for penalty parameter c .

3. Store the optimized Ansatz parameters θ_i , initialize $\phi_i := \theta_i$, and increment $i \rightarrow i + 1$.
In parallel:
 - (a) Return to step 2

AND

- (b) For the non-Hermitian Hamiltonian H_N , determine the Ansatz parameters ϕ_i that correspond to the i^{th} eigenstate via optimization of the pseudovariance objective function

$$\langle \psi(\phi_i) | H_N^\dagger H_N | \psi(\phi_i) \rangle - |\langle \psi(\phi_i) | H_N | \psi(\phi_i) \rangle|^2. \quad (6)$$

4. Proceed until $i = N + 1$.

Hybrid Quantum-Classical Implementation

To implement the aforementioned qDRIVE algorithm as a hybrid quantum-classical approach, we begin by generating the Ansatz wavefunction as a quantum circuit according

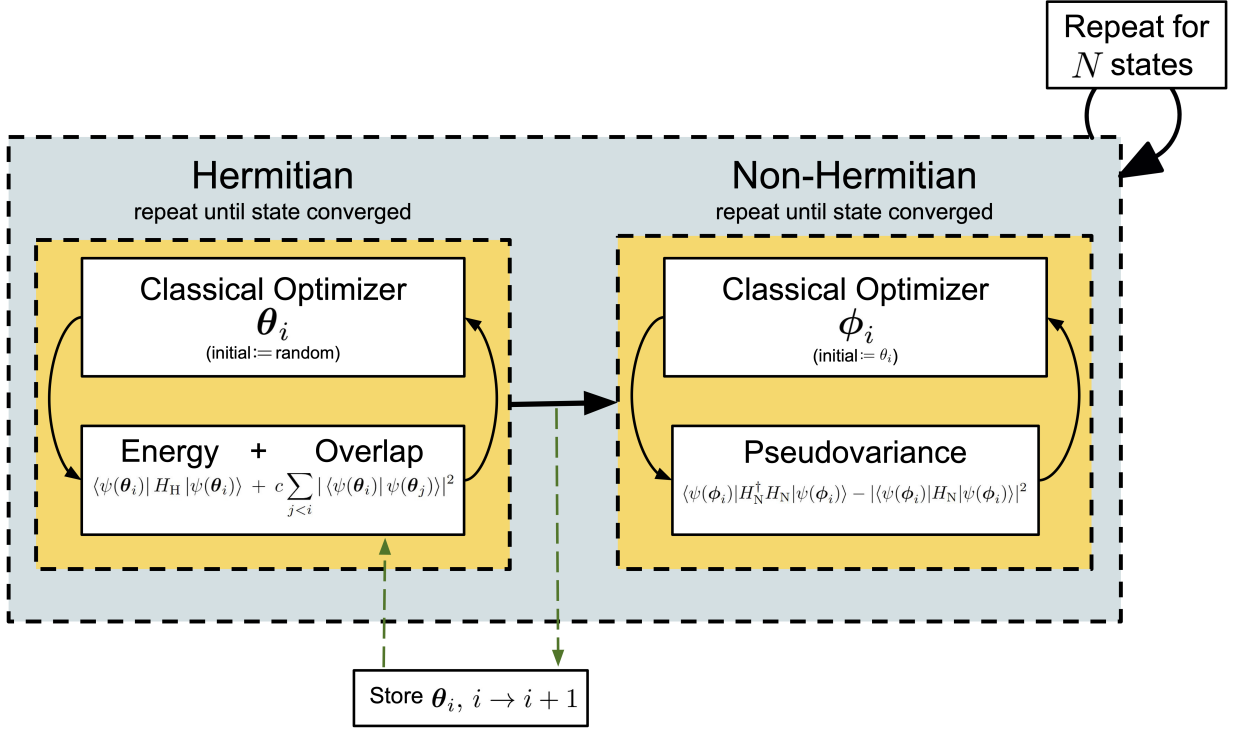


Figure 1: Schematic of the qDRIVE algorithm.

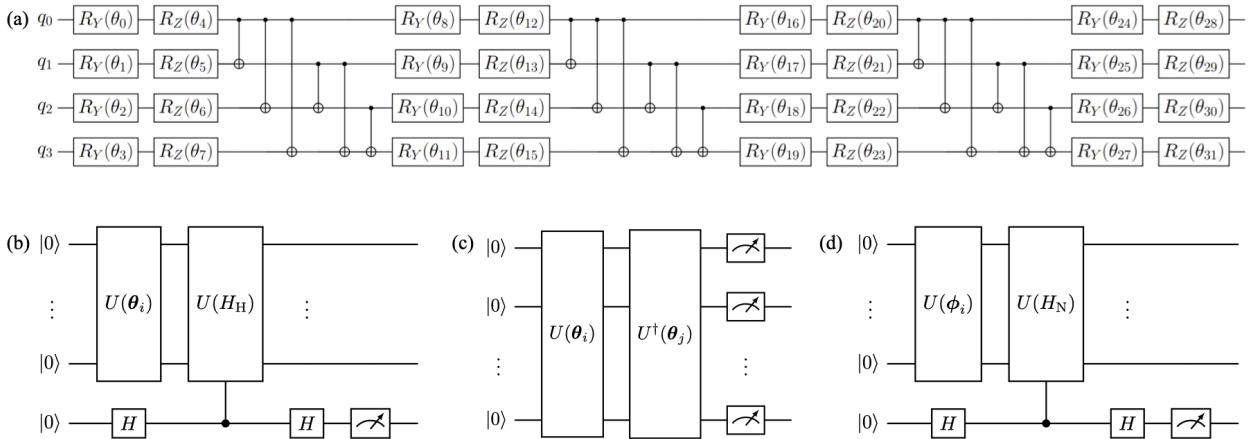


Figure 2: Quantum circuits for (a) the three-layer efficient $SU(2)$ Ansatz, (b) the Hadamard test for estimation of the expectation value of Pauli word components of the Hermitian Hamiltonian $\text{Re}(\langle U(H_H) \rangle)$, (c) the overlap between two states $\langle \psi(\theta_j) | \psi(\theta_i) \rangle = \langle \bar{0} | U^\dagger(\theta_j) U(\theta_i) | \bar{0} \rangle$, and (d) the Hadamard test for estimation of the expectation value of Pauli word components of the non-Hermitian Hamiltonian $\text{Re}(\langle U(H_N) \rangle)$.

to conventional VQE techniques,^{55–58} in which the Ansatz wavefunction consists of a series of unitary gates parametrized by m angles θ_i for eigenstate i , $|\psi(\theta_i)\rangle = U(\theta_i)|\bar{0}\rangle = U(\theta_{i_m})U(\theta_{i_{m-1}})\cdots U(\theta_{i_1})|\bar{0}\rangle$, where the form of the Ansatz is chosen to sufficiently balance expressibility and circuit depth. To meet these requirements, here we employ the three-layer efficient SU(2) Ansatz depicted in Fig. 2(a) with parameters initialized as pseudorandom angles in the domain $\theta_{i_o} \in [-\pi, \pi]$ for $o \in [1, m]$.

Eigenstate identification for the Hermitian Hamiltonian H_H is then performed via variational quantum deflation (VQD),¹⁰ in which the ground state and successively identified eigenstates are determined via VQE of an iteratively deflated Hamiltonian. Specifically, the Hermitian Hamiltonian H_H is represented as a weighted sum of a set of unitary terms amenable to encoding on a q -qubit quantum processor, here the q -qubit Pauli decomposition

$$M = \sum_{k_1=1}^4 \sum_{k_2=1}^4 \cdots \sum_{k_q=1}^4 C_{k_1, k_2, \dots, k_q} P_{k_1, k_2, \dots, k_q} \quad (7)$$

$$C_{k_1, k_2, \dots, k_q} = \text{Tr}(MP_{k_1, k_2, \dots, k_q}) \quad (8)$$

$$P_{k_1, k_2, \dots, k_q} = s_{k_1} \otimes s_{k_2} \otimes \cdots \otimes s_{k_q} \quad (9)$$

where P_{k_1, k_2, \dots, k_q} denotes a Pauli word comprised of Pauli gates $s_{k_l} \in \{I, X, Y, Z\}$ for $j = 1, 2, \dots, q$

$$I = \begin{bmatrix} 1 & 0 \\ 0 & 1 \end{bmatrix}, \quad X = \begin{bmatrix} 0 & 1 \\ 1 & 0 \end{bmatrix}, \quad Y = \begin{bmatrix} 0 & -i \\ i & 0 \end{bmatrix}, \quad Z = \begin{bmatrix} 1 & 0 \\ 0 & -1 \end{bmatrix}. \quad (10)$$

The objective function Eq. (5) is then estimated on the quantum processor using the decomposition at values of θ_i selected by a classical optimizer to converge towards the optimal values associated with the Hermitian Hamiltonian eigenstates: The classically expensive tasks of expectation value $\langle \psi(\theta_i) | H_H | \psi(\theta_i) \rangle$ and overlap $|\langle \psi(\theta_i) | \psi(\theta_j) \rangle|^2$ estimation are performed on the quantum processor via the Hadamard test shown in Fig. 2(b) or a direct product of

qubit measurements in the basis of each Pauli word for the former and the SWAP test,^{99,100} the destructive SWAP test,^{101,102} or the low-depth overlap method^{10,103} (shown in Fig. 2(c)) for the latter; and the classically efficient task of optimization is performed on the classical processor, ensuring the choice of classical optimizer suits the degree of noise associated with the quantum measurements and the choice of a penalty parameter c weighs sufficient deflation of the Hamiltonian with ease of the optimization.¹³ According to these considerations, here we employ a penalty parameter of $c = 100$ with 2^9 maximum optimization iterations for all classical optimizations, using COBYLA¹⁰⁴ (Constrained Optimization BY Linear Approximation, initial variable change $P_{\text{beg}} = 1$) in the absence of noise and the NFT method¹⁰⁵ (the Nakanishi-Fujii-Todo method, maximum function evaluations $f_{\text{max}} = 2^{11}$ and reset interval $R = 32$) in the presence of noise.

To converge the parameters associated with the Hermitian Hamiltonian eigenstates θ_i to the parameters associated with the non-Hermitian Hamiltonian eigenstates ϕ_i , we employ a hybrid quantum-classical approach to pseudovariance optimization. We decompose the operators required for evaluation of the pseudovariance objective function Eq. (6) H_N and $H_N^\dagger H_N$ according to the Pauli decomposition Eq. (7), employ the quantum processor to estimate their expectation values (see example in Fig. 2(d)), and identify the optimal parameters ϕ_i using a classical optimizer suitable in both noiseless and noisy conditions, here Py-BOBYQA^{106,107} (Bound Optimization BY Quadratic Approximation in Python, maximum function evaluations $f_{\text{max}} = 2^{10}$, requested maximum pseudovariance tolerance $f_{\text{tol}} = 0.05$, maximum full retrials to reach tolerance $u = 3$, and initial trust region radius $R_{\text{beg}} = 1$).

To reduce variance between instances of qDRIVE and thereby increase the robustness of the algorithm, the aforementioned procedure is executed as a batch of \mathcal{B} runs (here $\mathcal{B} = 8$). Duplicate states identified within a single run are omitted where the overlap between states is above a set tolerance, and the i^{th} eigenstate of H_N with the lowest value of the pseudovariance across batches is considered the optimal representative of the state. Nonresonant, diverging,

and indifferent states⁹² are then omitted through analysis of the eigenspectrum to produce the terminal list of resonances.

Given the asynchronicity of and minimal communication between the aforementioned Hermitian and non-Hermitian Hamiltonian eigenstate identification tasks, high-throughput computing (HTC)⁷²⁻⁷⁸ is used to minimize wall time to completion of the qDRIVE algorithm, with underlying classical computing tasks executed in parallel according to the directed acyclic graph illustrated in Fig. 3. For each run, one classical processor identifies the ground state of the Hermitian Hamiltonian $\psi(\theta_1)$, which initiates identification of the first eigenstate of the non-Hermitian Hamiltonian $\psi(\phi_1)$ on one processor and identification of the first excited state of the Hermitian Hamiltonian $\psi(\theta_2)$ on another. Convergence of the first excited state of the Hermitian Hamiltonian $\psi(\theta_2)$ then spurs identification of the second excited state of the non-Hermitian Hamiltonian $\psi(\phi_2)$ and identification of the second excited state of the Hermitian Hamiltonian $\psi(\theta_3)$ and so on, incrementing $i := i + 1$ and proceeding until all N eigenstates of H_N have been identified. The set of N eigenstates of H_N for each run $\{\psi(\phi_i)\}$ are then communicated to a single processor per run to pool information and finally on a single processor per batch to perform post-processing and visualization. The opportunity for parallelism offered by the directed acyclic graph may be paired with further parallelisms presented by the structure of the system under study. For example, where both the potential of interest V_0 and CAP V_{CAP} are of shared even parity, the eigenstates they support must also be of well-defined parity such that even and odd states may be constructed independently; where applicable, this parallelism (i) reduces the number of basis states that must be represented on the quantum processor for a given accuracy by half, which amounts to a reduction of the qubit count by one, and (ii) enables classical tasks to be divided into two identical copies of the same directed acyclic graph (one for each basis, odd and even), which reduces the wall time by half. These wall time improvements are obtained at the trade-off of a larger number of quantum circuit evaluations and classical processors, respectively. Additionally, this divided consideration of even and odd basis states simplifies

the optimization surface and ensures only basis states of suitable parity contribute to the qDRIVE-optimized state.

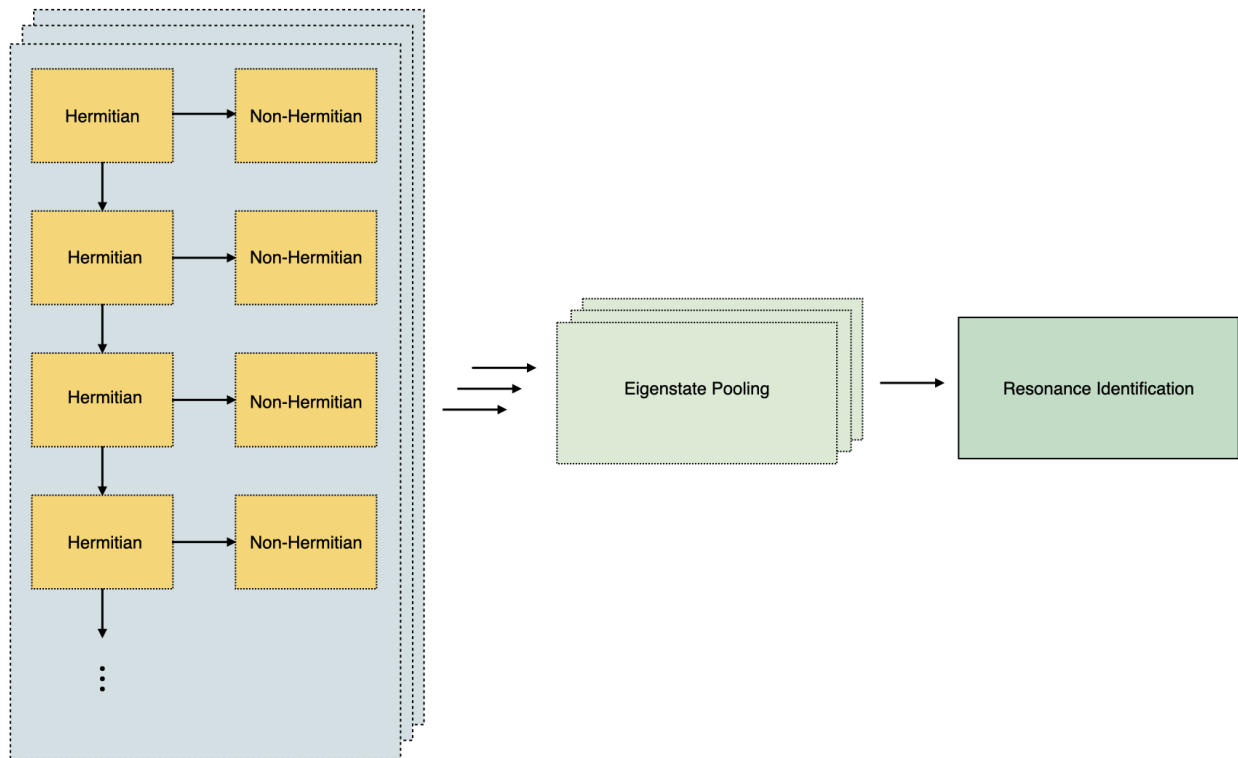


Figure 3: Schematic for implementation of qDRIVE with HTC resources. Each batch (blue rectangles) begins with identification of the ground state of the Hermitian Hamiltonian on an individual classical processor), which spawns both identification of a corresponding eigenstate of the non-Hermitian Hamiltonian on another classical processor and identification of the next excited state on yet another classical processor (yellow rectangles). For each batch, upon completion all resonances are pooled into a single file (lime rectangles), and finally sorted among all batches to identify the result for each resonance with the lowest pseudovariance (green rectangle).

Near-Term Error Mitigation

To facilitate the implementation of qDRIVE on near-term quantum computers, we employ readout and gate error mitigation in conjunction with special consideration of the identity Pauli word.

Readout Error Mitigation Elementary readout error mitigation is performed via matrix inversion, in which the true statistics of ancilla measurement are inferred from noisy statistics^{85–87} (see also advanced techniques⁸⁴ such as twirled readout error extinction^{108,109} to counteract noise-induced bias). Where the noisy expectation vector \vec{N} is related to the true expectation vector \vec{T} by

$$\begin{bmatrix} N_0 \\ N_1 \end{bmatrix} = \begin{bmatrix} T_0 \\ T_1 \end{bmatrix} \begin{bmatrix} p_{00} & p_{01} \\ p_{10} & p_{11} \end{bmatrix} \quad (11)$$

where the 0th and the 1st element of each vector correspond to the probability the ancilla is measured in the $|0\rangle$ and $|1\rangle$ state, respectively, and where p_{ij} is the probability the qubit is in true state i but measured in state j in the presence of noise (determined through system benchmarking¹¹⁰); the true expectation vector components are estimated as

$$T_0 = \frac{N_0 - p_{10}}{p_{00} - p_{10}}, \quad T_1 = \frac{N_1 - p_{01}}{p_{11} - p_{01}} \quad (12)$$

according to solution of the system of equations given normalization of the true expectation vector $T_0 + T_1 = 1$ as expected of a classical probability.

Gate Error Mitigation Gate error mitigation is performed via hybrid exponential-linear three-point zero-noise extrapolation (ZNE).^{88,90,91} According to standard ZNE, each circuit result x_λ is extrapolated to its zero-noise counterpart $\lambda = 0$ based on the original result of the circuit $\lambda = 1$ and artificially increased-error iterations of the circuit with $(\lambda - 1)/2$ repetitions of each gate and its inverse. We thus fit x_1 , x_3 , and x_5 to the exponential function

$$x_\lambda \approx A + Be^{C\lambda} \quad (13)$$

via solution of equations for the constants A, B, C to yield the zero-noise extrapolated circuit result⁹¹

$$x_0 = x_1 + \frac{x_1 - x_3}{\beta^2 + \beta}, \quad \beta = \sqrt{\frac{x_3 - x_5}{x_1 - x_3}}. \quad (14)$$

Importantly, the resulting zero-noise result x_0 is physically realizable ($x_0 \in \mathcal{R}$) if and only if $(x_3 - x_5)/(x_1 - x_3) > 0$ (*i.e.*, where x_λ is monotonic for the three points considered). We therefore employ physically motivated linear approximations where monotonicity is violated to within statistical significance as detailed in the appendix.

Identity Pauli Word Additionally, we make the simple recognition that the expectation value of the identity Pauli word $I^{\otimes q}$ is analytically known to be unity

$$\langle \psi | I^{\otimes q} | \psi \rangle = \langle \psi | \psi \rangle = 1 \quad (15)$$

for all normalized states ψ , such that the expectation value need not be estimated on the quantum processor. This small point ensures accurate evaluation of the term free of the vicissitudes of readout or gate error, of particular importance for the investigation of chemical Hamiltonians (and associated pseudovariances) for which its associated weight in the Pauli decomposition Eq. (7) is relatively large.

Model System

To demonstrate the power of the qDRIVE algorithm, we present the method as applied to a benchmark potential designed to model resonances associated with diatomic predissociation and molecular scattering collisions⁶²

$$V_0(x) = \left(\frac{1}{2}x^2 - J\right) e^{-\lambda x^2} + J \quad (16)$$

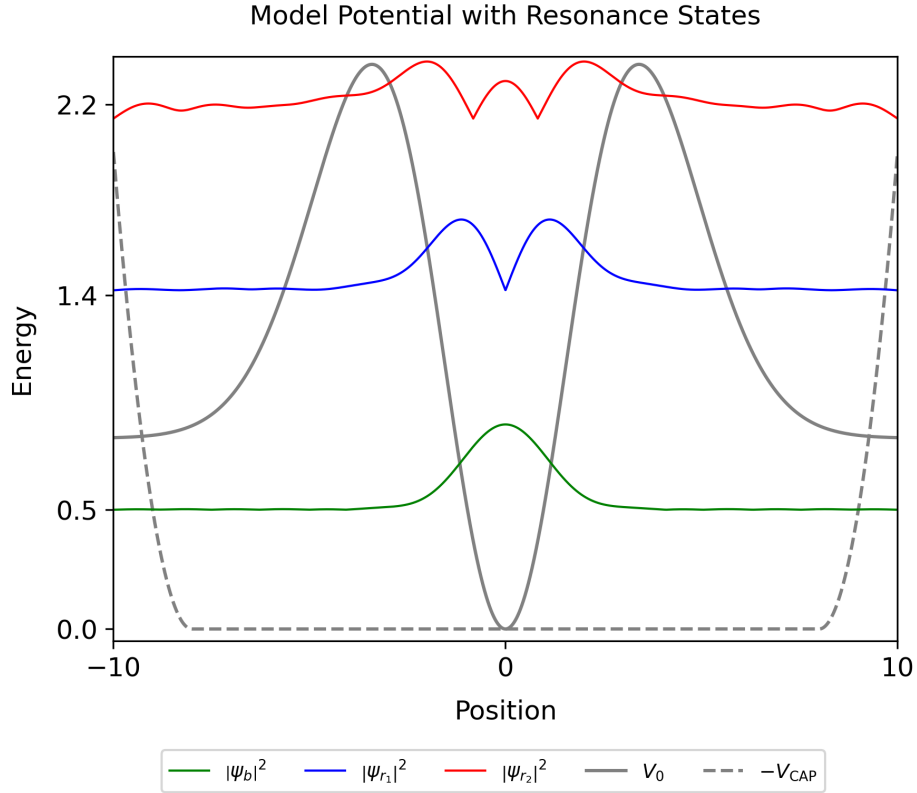


Figure 4: Benchmark potential energy surface V_0 (solid gray line), which supports a bound state ψ_b and two resonances ψ_{r_1} and ψ_{r_2} (solid green, blue, and red lines, probability density shown), here termed the bound state, first resonance, and second resonance, respectively, shown as computed via the established classical CAP method of exact diagonalization where purely outgoing boundary conditions are imposed by a complex absorbing potential V_{CAP} (dashed gray line, shown as $-V_{\text{CAP}}$). Each state's probability density is vertically shifted by the value of the real part of its energy $\text{Re}(E)$.

where $\lambda = 0.1$ and $J = 0.8$ (arbitrary units by convention), with purely outgoing boundary conditions imposed via a quadratic CAP

$$V_{\text{CAP}}(x) = \begin{cases} 0 & |x| \leq x_0 \\ -\frac{1}{2}(|x| - x_0)^2 & |x| > x_0 \end{cases} \quad (17)$$

where $x_0 = 8$ au, as illustrated in Fig. 4. To aid direct comparison to literature results, we specifically examine the resonance near $\text{Re}(E_{r_2}) = 2.13$ investigated by Bian et al. with the direct measurement method.⁵³ To demonstrate the breadth of the method, we additionally employ qDRIVE to identify the bound state near $E_b = 0.502$ and the narrower resonance near $\text{Re}(E_{r_1}) = 1.42$. Simulations shown here are performed for a Hamiltonian implemented in position-space representation in the domain $x \in [-x_{\text{max}}, x_{\text{max}}]$ with $x_{\text{max}} = 10$ and 2^{12} grid-points, a kinetic energy operator computed according to the second-order finite differencing gradient, and a basis set comprising of 2^q sinusoidal basis states of length $L = 2x_{\text{max}}$

$$\phi_k(x) = \sqrt{\frac{2}{L}} \sin\left(\frac{w\pi}{L}\left(x - \frac{L}{2}\right)\right) \quad (18)$$

of either even $w = 1, 2, 3, \dots$ or odd $w = 2, 4, 6, \dots$ symmetry.

Quantum Simulation and Experimental Tests

All codes for quantum simulation and experimental tests have been made available publicly under an open-source license from Github¹¹¹ using IBM Qiskit.¹¹² The statevector simulator is used to examine qDRIVE in the absence of noise; the Aer simulator, in the presence of only statistical shot noise; and a custom simulator, in the presence of statistical shot noise, readout noise, and gate noise. IBM Falcon r4T processors are used to examine the efficacy of real quantum computers for the most quantum-processor-intensive stage of qDRIVE (namely, pseudovariance minimization).

In simulations, where statistical shot noise is incorporated, $n = 10^5$ shots are taken per

quantum circuit. An additional order of magnitude of shots is employed for final comparison of results between runs. Where readout and gate error are included, the noise model for thermal relaxation at time t incorporates both the generalized amplitude damping channel Kraus matrices

$$K_0 = \sqrt{1-p} \begin{bmatrix} 1 & 0 \\ 0 & \sqrt{1-\gamma_1} \end{bmatrix}, K_1 = \sqrt{1-p} \begin{bmatrix} 0 & \sqrt{\gamma_1} \\ 0 & 0 \end{bmatrix}, \quad (19)$$

$$K_2 = \sqrt{p} \begin{bmatrix} 1 & 0 \\ 0 & \sqrt{1-\gamma_1} \end{bmatrix}, K_3 = \sqrt{p} \begin{bmatrix} 0 & \sqrt{\gamma_1} \\ 0 & 0 \end{bmatrix}, \quad (20)$$

$$\gamma_1 = 1 - e^{-t/T_1}, \quad (21)$$

where p is the equilibrium excited state population and T_1 is the generalized amplitude damping relaxation time, and the phase damping model Kraus matrices

$$K_0 = \begin{bmatrix} 1 & 0 \\ 0 & \sqrt{1-\gamma_2} \end{bmatrix}, K_1 = \begin{bmatrix} 0 & 0 \\ 0 & \sqrt{\gamma_2} \end{bmatrix} \quad (22)$$

$$\gamma_2 = 1 - e^{-t/T_2}, \quad (23)$$

where T_2 is the phase damping relaxation time. The local one- and two-qubit depolarizing error is then described by the error channel

$$E(\rho) = (1-p_d)\rho + p_d \text{Tr}[\rho] \frac{I}{2^d} \quad (24)$$

for d -qubit gate error probability p_d . In the custom simulator model of IBM Torino, qubit and processor specifications are hard-coded to approximate the contemporary properties of the quantum processor, including system basis gates and qubit-specific one- and two-qubit gate errors, readout errors, T_1/T_2 times, and gate times. To reduce simulation cost, only five qubits of the full IBM Torino system are simulated to accommodate a maximal four-qubit

Ansatz and a single ancilla. Quantum processors with specifications beyond those of IBM Torino are simulated using the same custom simulator with a gate noise reduction factor applied to the one- and two-qubit gate error probabilities p_1 and p_2 and a qubit longevity factor that represents the order of magnitude of the T_1 relaxation time where the leading digit of T_1 and the ratio between the T_1 and T_2 relaxation times is held fixed. For example, where the IBM Torino relaxation times T_1 and T_2 are approximated as 70 μs and 50 μs , respectively, a qubit longevity factor of 100 μs implies relaxation times T_1 and T_2 of 700 μs and 500 μs , respectively. Infinite qubit longevity factors correspond to the absence of thermal relaxation.

In experimental tests on real quantum processors, the most computationally intensive stage of qDRIVE for the quantum processor, namely, pseudovariance minimization, is tested on five-qubit IBM Falcon r4T quantum processors Quito, Belem, and Lima. Device specifications, including qubit relaxation times and gate error rates, are provided for reference in Table 1. To isolate error due to pseudovariance minimization from that of variational quantum deflation (VQD), Ansatz parameters are randomly initialized in the domain $\theta_{i_o} \in [-\pi, \pi]$ where $o \in [1, m]$. A two-local circuit with R_x and R_y rotation gates is employed with full entanglement between qubits provided by CNOT gate layers in order to balance Ansatz expressibility with quantum processor cost where applicable. Energies are computed for one- and two-qubit Hamiltonians represented in a sinusoidal basis using a shot number of $n = 10^4$ on the quantum processor and COBYLA¹⁰⁴ (tolerance 10^{-3} , maximum iteration number 15) on the classical processor. Given limited quantum processing resources, real quantum computer tests are automatically executed on the least occupied quantum processor and in such tests no error mitigation methods are employed.

Results are reported in terms of energies computed at the level of quantum simulation or quantum computation used and eigenstate probability densities are visualized where relevant with the statevector simulator. To evaluate the success of qDRIVE, qDRIVE’s accuracy, robustness, and computational cost are compared to that of two established classical resonance

identification techniques: (1) the established classical CAP resonance identification method in which resonances are determined via exact diagonalization of $H_N = H_H + iV_{\text{CAP}}$,^{35–39} and (2) the established classical complex scaling method in which resonances are determined via θ trajectories of the complex-scaled Hamiltonian.^{40,41,53} Classical CAP method results are presented for identical basis sets to that of qDRIVE for direct comparison, and classical complex scaling method results are presented for a basis set of five orthogonalized Gaussian basis states $\chi_k(\alpha) = \exp(-\alpha_k x^2)$ with $\alpha_k = 0.65 \cdot 0.45^k$ where $k = 0, 1, 2, 3, 4$ for comparison to the literature solution of ref. 53.

Results

The interlaced quantum computing/HTC qDRIVE approach was found to accurately identify all resonance energies considered for the benchmark resonance model of molecular predissociation Eq. (16) as compared to established classical resonance identification techniques. As shown in Table 2, the error of the bound-state energy E_b , the first-resonance energy E_{r_1} , and the second-resonance energy E_{r_2} relative to the established classical CAP method results was found to remain below 1% in all statevector simulations for two- to four-qubit Ansätze. Additionally, the relative error was observed to be as low as $O(10^{-5}\%)$ for the highest qubit-number statevector simulation considered, indicative of the success of the method in the absence of shot noise and readout and gate error. In experiments with the Aer simulator that included shot noise, the relative error remained below 1% in all simulations with the exception of a relative error of 2.8% for E_{r_2} where a three-qubit Ansatz was employed, which was also associated with larger componentwise error of $\text{Im}(E_b)$ and $\text{Im}(E_{r_1})$. As expected, in custom simulations of IBM Torino that included readout and gate error, the relative error was larger but still in the vicinity of classical CAP method results, with an error as low as 0.91% for E_{r_1} with a two-qubit Ansatz and as high as 35% for the same energy E_{r_1} with a three-qubit Ansatz, which suggests qDRIVE may be already implemented as specified with existing quantum computing systems where the error tolerance is acceptable. qDRIVE

Table 1: Specifications of IBM Falcon r4T quantum processor devices (version in parenthesis) employed in experiments, as of September 14, 2023, from IBM Qiskit¹¹². Values are reported in microseconds for relaxation times T_1 and T_2 , nanoseconds for two-qubit gate times, and with implied multiplicative factors of 10^{-2} , 10^{-4} , 10^{-4} , 10^{-4} , and 10^{-3} for readout assignment, I , \sqrt{X} , X , and CNOT error rates, respectively.

Device	Qubit	T_1	T_2	Error					Gate Time
				Readout	I	\sqrt{X}	X	CNOT	
Quito (1.1.45)	0	112.5	139.23	3.340	2.437	2.437	2.437	0_1:0.03884	0_1:234.667
								1_3:0.00958	1_3:334.222
	1	106.41	101.49	3.640	2.726	2.726	2.726	1_2:0.01122	1_2:298.667
								1_0:0.03884	1_0:270.222
	2	63.66	37.37	7.640	3.474	3.474	3.474	2_1:0.01122	2_1:263.111
							3_4:0.01469	3_4:277.333	
	3	58.45	18.14	3.920	2.713	2.713	2.713	3_1:0.00958	3_1:369.778
								3_1:0.00958	3_1:369.778
	4	70.44	131.29	4.05	2.767	2.767	2.767	4_3:0.01469	4_3:312.889
								4_3:0.01469	4_3:312.889
Belem (1.2.12)	0	116.9	135.85	2.740	2.104	2.104	2.104	0_1:0.01478	0_1:810.667
								1_3:0.00669	1_3:440.889
	1	93.12	92.11	1.960	4.920	4.920	4.920	1_2:0.00586	1_2:419.556
								1_0:0.01478	1_0:775.111
	2	58.22	47.91	1.65	1.976	1.976	1.976	2_1:0.00586	2_1:384.00
							3_4:0.00908	3_4:526.222	
	3	88.4	94	2.63	2.721	2.721	2.721	3_1:0.00669	3_1:405.333
								3_1:0.00669	3_1:405.333
	4	58.15	45.07	1.73	5.656	5.656	5.656	4_3:0.00908	4_3:490.667
								4_3:0.00908	4_3:490.667
Lima (1.0.52)	0	113.67	160.08	1.96	7.567	7.567	7.567	0_1:0.00662	0_1:305.778
								1_0:0.00662	1_0:341.333
	1	93.43	131.71	1.740	5.44	5.44	5.44	1_3:0.01152	1_3:497.778
								1_2:0.00695	1_2:334.222
	2	69.01	99.69	2.06	7.334	7.334	7.334	2_1:0.00695	2_1:298.667
							3_4:0.01476	3_4:519.111	
	3	59.08	91.58	3.85	2.367	2.367	2.367	3_1:0.01152	3_1:462.222
								3_1:0.01152	3_1:462.222
	4	16.13	16.17	4.43	6.514	6.514	6.514	4_3:0.01476	4_3:483.556
								4_3:0.01476	4_3:483.556

Table 2: (a) Bound and resonance state energies E_b , E_{r_1} , and E_{r_2} computed according to qDRIVE for a q -qubit Ansatz via the quantum simulators (Sim.) Statevector, Aer, and IBM Torino, as compared to the result of the classical CAP method according to (b) percent relative error $\mathcal{E} = |z' - z| / |z|$.

q	Sim.	E_b	E_{r_1}	E_{r_2}
2	Classical CAP Method	$0.623 - 2.63 \cdot 10^{-3}i$	$1.61 - 4.15 \cdot 10^{-2}i$	$2.36 - 5.83 \cdot 10^{-3}i$
	Statevector	$0.623 - 2.78 \cdot 10^{-3}i$	$1.61 - 4.26 \cdot 10^{-2}i$	$2.34 - 1.22 \cdot 10^{-2}i$
	Aer	$0.619 - 2.97 \cdot 10^{-3}i$	$1.61 - 3.97 \cdot 10^{-2}i$	$2.35 - 7.13 \cdot 10^{-3}i$
	Torino	$0.685 - 2.37 \cdot 10^{-3}i$	$1.61 - 5.62 \cdot 10^{-2}i$	$2.20 - 1.29 \cdot 10^{-2}i$
3	Classical CAP Method	$0.505 - 2.02 \cdot 10^{-5}i$	$1.43 - 1.61 \cdot 10^{-4}i$	$2.15 - 2.04 \cdot 10^{-2}i$
	Statevector	$0.504 - 2.48 \cdot 10^{-5}i$	$1.43 - 1.44 \cdot 10^{-4}i$	$2.14 - 1.00 \cdot 10^{-2}i$
	Aer	$0.505 + 2.43 \cdot 10^{-4}i$	$1.44 + 2.60 \cdot 10^{-4}i$	$2.09 - 2.64 \cdot 10^{-2}i$
	Torino	$0.562 + 2.22 \cdot 10^{-3}i$	$1.92 - 8.85 \cdot 10^{-2}i$	$2.18 - 1.09 \cdot 10^{-2}i$
4	Classical CAP Method	$0.502 - 9.98 \cdot 10^{-11}i$	$1.42 - 3.60 \cdot 10^{-5}i$	$2.12 - 1.18 \cdot 10^{-2}i$
	Statevector	$0.502 - 1.23 \cdot 10^{-7}i$	$1.42 - 4.03 \cdot 10^{-5}i$	$2.13 - 4.63 \cdot 10^{-4}i$

q	Sim.	\mathcal{E}_b	\mathcal{E}_{r_1}	\mathcal{E}_{r_2}
2	Statevector	0.02%	0.07%	0.89%
	Aer	0.64%	0.11%	0.43%
	Torino	9.95%	0.91%	6.79%
3	Statevector	0.20%	0.0012%	0.67%
	Aer	0.05%	0.70%	2.80%
	Torino	11.30%	34.82%	1.46%
4	Statevector	0.000024%	0.00030%	0.71%

results for the second resonance energy E_{r_2} were also found to be accurate relative to the literature classical complex scaling method result from ref. 53 of $E = 2.1265 - 0.0203i$. As expected, the accuracy of qDRIVE relative to the established classical complex scaling resonance identification technique was found to increase as the basis set size increased, with a relative error of 10.0%, 10.5%, and 3.5% for two-qubit statevector, Aer, and Torino, respectively; 0.8%, 1.7%, and 2.6% for three-qubit statevector, Aer, and Torino, respectively; and 0.9% for four-qubit statevector. Note the qDRIVE simulations were also found to be highly robust relative to established classical resonance identification techniques, as the bound and resonance states were identified in 100% of the quantum simulations for the number of batch runs considered, in full agreement with the robustness of classical CAP and classical complex scaling methods.

Results of the real quantum computer experiments, shown in Table 3, indicate that pseudovariance minimization successfully yielded complex energies near eigenvalues of the Hamiltonian. Both eigenvalues of the one-qubit Hamiltonian were identified, with a relative error of 17.0% and 5.1% relative to the classical CAP method result. The two complex energies of the two-qubit Hamiltonian with a real part closest to that of the scattering r_1 and r_2 resonances observed for larger basis sets were likewise measured with 30.5% and 8.9% relative error relative to the classical CAP method of exact diagonalization of the same Hamiltonian, respectively. As expected, the resonance energies were therefore within the vicinity of but with a higher degree of relative error than statevector, error-mitigated Aer, and error-mitigated simulated IBM Torino resonance energies for the system examined in Table 2.

qDRIVE was also found to successfully produce probability densities consistent with classical CAP method results for all resonances considered, as shown in Fig. 5 for a three-qubit Ansatz. Probability densities from statevector simulations closely agreed with classical CAP method results for the bound state and first resonance, with a higher discrepancy in the second resonance that may be attributable to the underlying deflation procedure given

Table 3: Energies of selected states computed via qDRIVE pseudovariance minimization of a randomly initiated q -qubit Ansatz on IBM Falcon r4T Quito, Lima, and Belem processors, with percent relative error \mathcal{E} calculated relative to the classical CAP method of exact diagonalization of the corresponding Hamiltonian. Note the two-qubit classical CAP method values are distinct from those of Table 2 as a combined even/odd basis set is employed.

q	Classical CAP Method	IBM Falcon r4T	\mathcal{E}
1	$0.55 + 0.0000i$	$0.54 + 0.093i$	17.0%
	$2.22 + 0.0000i$	$2.11 + 0.0248i$	5.1%
2	$1.56 + 0.0698i$	$1.39 - 0.3745i$	30.5%
	$2.26 - 0.0034i$	$2.06 - 0.007i$	8.9%

the high-lying nature of its corresponding Hermitian Hamiltonian eigenstate. Probability densities from Aer simulations were found to be accurate in the internal region of the potential, with a lower degree of accuracy than statevector, as expected due to the additional consideration of statistical noise. Consistent with the impact of further readout and gate noise, the greatest discrepancy between the qDRIVE-optimized and classical-CAP-method probability densities was observed for the custom simulations of IBM Torino; nonetheless, overall trends of localization of the bound state and resonances in the potential’s internal region and reduction in the outer region were preserved.

Increased gate noise reduction and qubit longevity factors were associated with lower pseudovariance and fidelity error of the qDRIVE-optimized resonances, as shown in Fig. 6 and Fig. 7. Both the pseudovariance and the fidelity error were found to approach their optimal zero value of zero as the gate noise reduction factor increased from 10^0 to 10^4 and the qubit longevity increased from 10^1 to ∞ μs , with fluctuations in keeping with the statistical nature of the simulations. An increase in the maximal value of the pseudovariance was also observed for states corresponding to higher-lying eigenstates of the Hermitian Hamiltonian in keeping with errors introduced by deflation.

Notably, convergence of the complex energies to their classical CAP method values was evident even where the pseudovariance and fidelity errors were far from their optimal zero values, as depicted in Figs. 8, 9, and 10 for a three-qubit Ansatz. As shown in Fig. 8,

Probability Density of qDRIVE-Optimized State

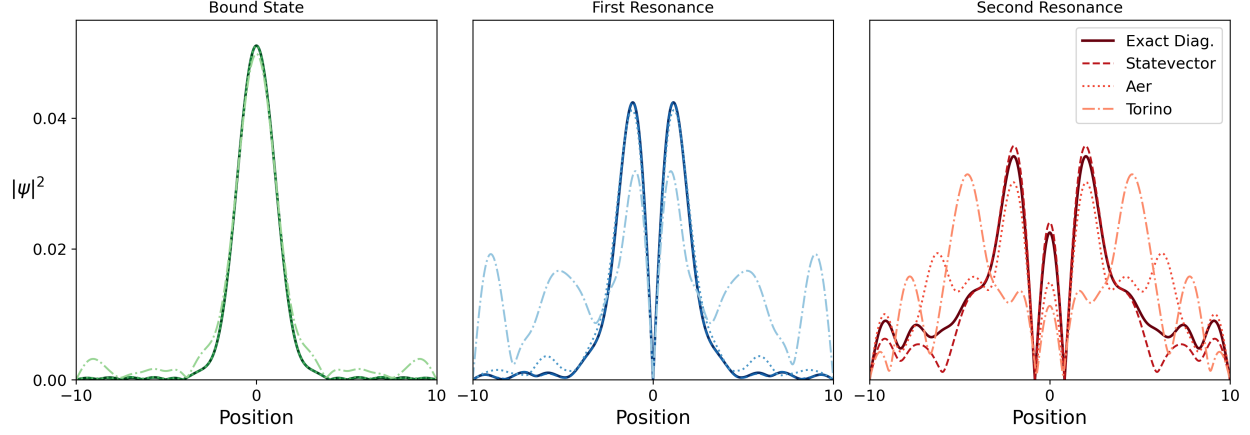


Figure 5: Probability density $|\psi|^2$ visualized in position space corresponding to the qDRIVE-optimized three-qubit Ansatz for the statevector (dashed lines), Aer (dotted lines), and Torino (dashed-dotted lines) simulators as compared to classical CAP method/exact diagonalization (solid lines) for the (left) bound state (green lines), (center) first resonance (blue lines), and (right) second resonance (red lines).

Pseudovariance of qDRIVE-Optimized State

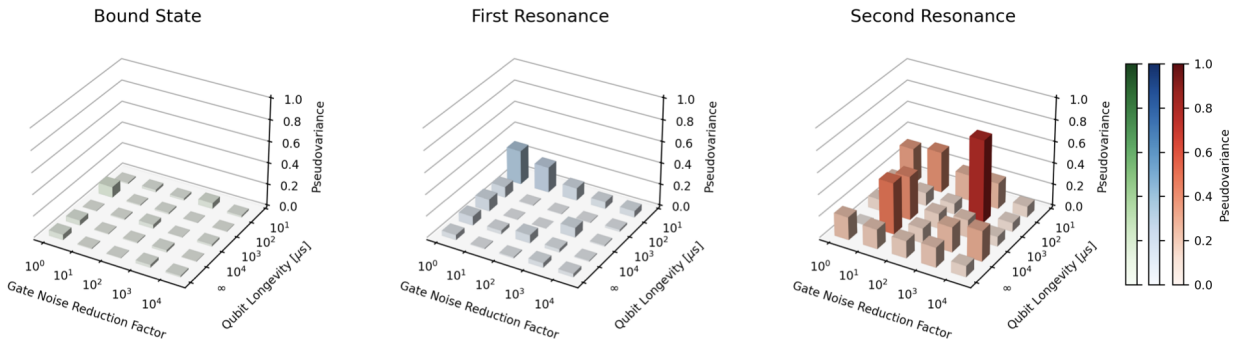


Figure 6: Pseudovariance Eq. (2) of the (left) bound state, (center) first resonance, and (right) second resonance as determined by qDRIVE with a three-qubit Ansatz as a function of the gate noise reduction and qubit longevity factors.

Fidelity Error of qDRIVE-Optimized State

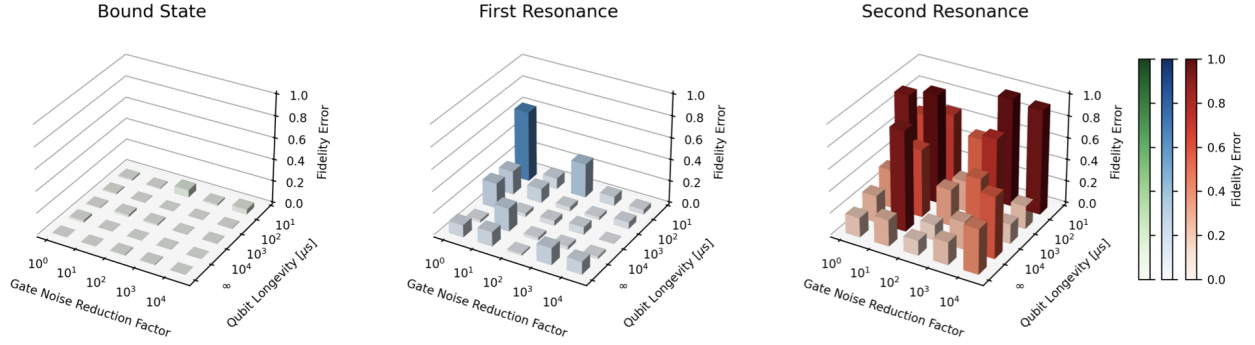


Figure 7: Fidelity error of the simulated qDRIVE-optimized (left) bound state, (center) first resonance, and (right) second resonance ψ_{Sim} as compared to the classical CAP method/exact diagonalization result ψ_{Exact} , $1 - |\langle \psi_{\text{Sim}} | \psi_{\text{Exact}} \rangle|^2$, for increasing gate noise reduction and qubit longevity factors.

the real part of the qDRIVE-optimized bound-state, first-resonance, and second-resonance energies closely agreed with the classical CAP method value for all gate noise reduction and qubit longevity factors considered, with imaginary parts with an absolute error within 0.1 regardless of gate noise for qubit longevity factors of at least 1000 μs , on the order of the millisecond times recently achieved on advanced 2D transmon qubits.¹¹³ The bound-state energy specifically was found to be nearly indistinguishable from the classical CAP method result at the resolution shown without magnification for qubit longevity factors of at least 10 μs , namely, on the order of IBM Torino relaxation times. As emphasized in Fig. 9, the

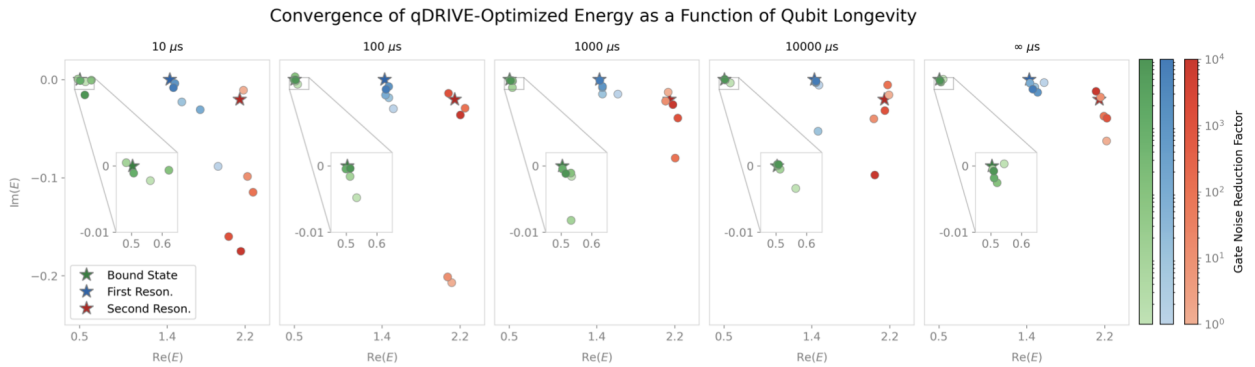


Figure 8: Approach of the bound-state (with magnification), first-resonance, and second-resonance energy (circles; green, blue, and red, respectively) to the corresponding classical CAP method/exact diagonalization energy (stars) with increased qubit longevity. Darker colors indicate higher gate noise reduction factor.

bound-state and first-resonance energies’ imaginary parts were accurate to within an absolute error of 0.1 for gate noise reduction factors of at least 10^0 and qubit longevity factors of at least $10 \mu\text{s}$, both of which are accessible with current IBM Torino systems. Consistent with trends in the pseudovariance and fidelity error, higher errors in the real and imaginary parts of the energy were observed for the second resonance associated with a higher-lying eigenstate of the Hermitian Hamiltonian. As shown in Fig. 10, weaker nonmonotonic convergence of the imaginary part of the qDRIVE-optimized energy to classical CAP method/exact diagonalization results was observed for the second resonance as the gate noise reduction factor increased, a correlation between repeated deflation and error emergence that suggests possible benefits of the future injection into qDRIVE of higher-accuracy VQD variants (such as the tangent-vector VQE method¹¹⁴) or variational algorithms for high-lying eigenstate identification (such as adaptive VQE-X⁹⁵).

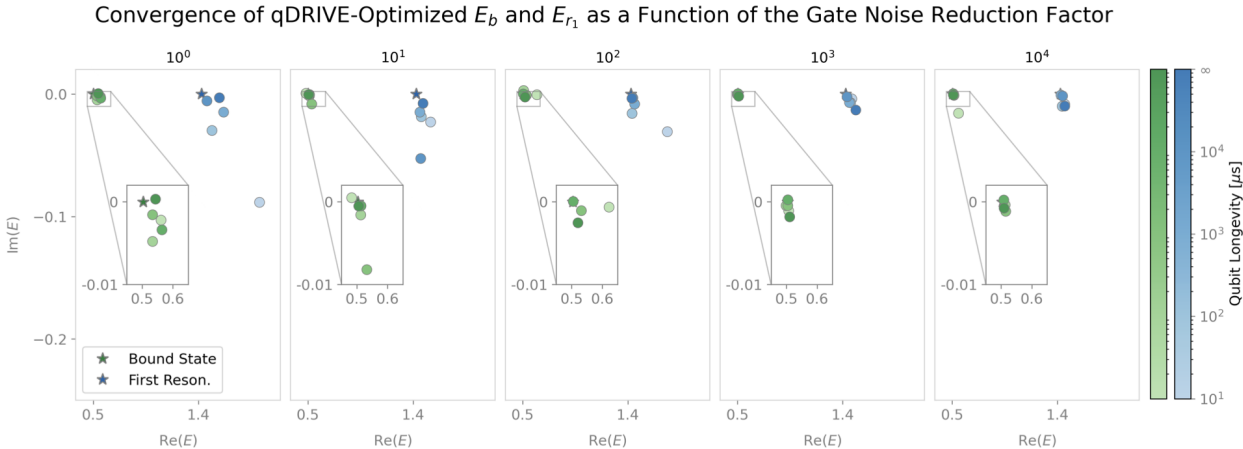


Figure 9: Progression of the energy of the bound state and first resonance (green and blue circles, respectively) towards the corresponding classical CAP method/exact diagonalization energy (green and blue stars, respectively) as the gate noise reduction factor increases. Darker colors indicate longer qubit longevity.

Discussion and Conclusion

The success of the proposed qDRIVE algorithm points to the potential efficiency and efficacy of a hybrid quantum computing/high-throughput computing (HTC) approach to chemistry.

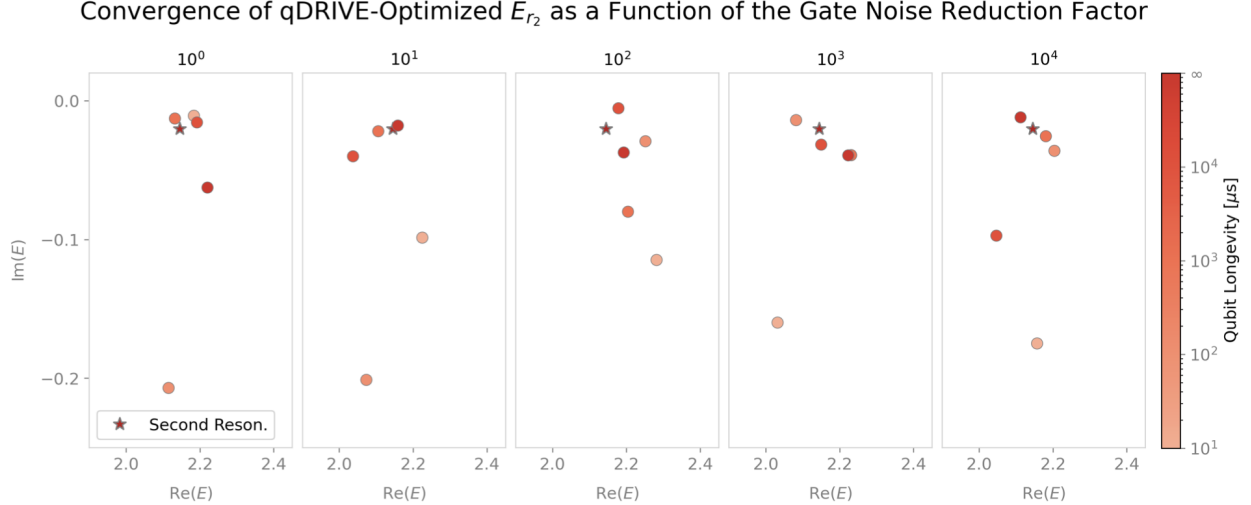


Figure 10: As in Fig. 9, for the second resonance.

qDRIVE’s ability to identify molecular resonance energies and wavefunctions in a benchmark potential on simulated noisy intermediate scale quantum (NISQ) computers invites its implementation on today’s quantum processors. Its projected accuracy for more advanced quantum processors suggests the algorithm may offer yet improved accuracy as quantum processors continue to develop. And, more broadly, qDRIVE’s success serves as a prototype for a wider family of heterogeneous quantum computing algorithms.

Making qDRIVE fully practical for systems beyond the small-scale systems considered here will require addressing the issue of Hamiltonian mapping. It is well-known that grid-based mappings, such as the method used here to represent the benchmark potential, feature a storage cost that grows exponentially with the grid size.^{56,115} Molecular electronic resonances^{32,116} may be able to circumvent this problem given the existence of alternative, scalable Hamiltonian mappings for electronic structure problems¹¹⁷ such as the renowned Jordan-Wigner¹¹⁸ and Bravyi-Kitaev¹¹⁹ fermion-qubit mappings. Additionally, where decompositions of the Hamiltonian and its products result in a large number of expectation values to be measured, a variety of methods currently under development may reduce the number of expectation values that need to be computed, and therefore reduce the overall cost of qDRIVE’s implementation. Classical shadow tomography,^{120–122} for example, allows

for the reconstruction of unmeasured expectation values based on the “shadow” of a smaller subset of measured values, and the method of commuting strings¹²³ allows for large numbers of expectation values to be computed with comparatively fewer quantum circuits.

An adaptive Ansatz approach offers a pathway to extend qDRIVE to larger-scale systems. qDRIVE’s observed ability to accurately identify resonance energies and wavefunctions suggests the three-layer efficient SU(2) Ansatz is sufficient for analysis of the benchmark molecular system of interest; however, a key question is how to maintain this expressibility and efficiency upon the addition of parameters and entanglement between large numbers of qubits. One possibility is ADAPT-VQE (Adaptive Derivative-Assembled Pseudo-Trotter Ansatz Variational Quantum Eigensolver), which has been seen to be a highly effective means to improve the scalability of VQE.¹²⁴ By optimizing both the parameters and form of the Ansatz, a variant of ADAPT-VQE has successfully enabled VQE on 127-qubit processors, including a 100-qubit study of the lattice Schwinger model.¹²⁵

The contracted quantum eigensolver (CQE)^{15,94,126,127} provides another pathway to expand qDRIVE to larger system sizes. As in ADAPT-VQE, CQE possesses the ability to modify an Ansatz until it suits the quantum system under study. However, unlike ADAPT-VQE, CQE’s two-body Ansatz construction method never calls for parameter reoptimization. This distinction, along with the structure of the contracted Schrödinger equation on which CQE relies, allows CQE to readily produce analytic gradients of the energy with respect to the Ansatz parameters. Thus, whereas ADAPT-VQE typically relies on gradient-free classical optimization algorithms such as COBYLA, CQE can capitalize on efficient gradient-based classical optimization algorithms that offer important cost savings where quantum resources remain scarce.

In established classical resonance identification techniques, the computational cost generally scales directly with the size of the Hamiltonian matrix. For example, the matrix diagonalizations frequently used in classical CAP and complex scaling methods^{62,128} scale as $O(N^3)$. In contrast, the computational cost of qDRIVE can scale independently of the

Hamiltonian matrix size. qDRIVE’s variational hybrid quantum-classical computing approach is expected to give qDRIVE a computational complexity akin to that of VQE,³ namely, the cost of identifying of a single state in qDRIVE is expected to scale as $O(|C_{\max}|^2 tp^{-2})$, where C_{\max} is the largest-magnitude coefficient of the Pauli decomposition Eq. (7), t is the number of terms in said decomposition, and p is the desired precision.² The cost comparison therefore suggests the value of a search for possible advantage in the large system limit, with the caveat that the quantum utility of variational quantum algorithms remains a topic of continued heated debate.^{57,58}

qDRIVE’s success invites the further development of integrated quantum computing and HTC approaches. The interconnection of high-performance computing (HPC) resources and quantum computers is an emerging hot topic in quantum information science, and much focus has been placed on distributed quantum computing systems based either on multiple quantum processing units working in concert or heterogeneous computing systems consisting of central processing units (CPUs), graphical processing units (GPUs), and quantum processing units (QPUs).⁶⁸⁻⁷⁰ The accomplishments here of qDRIVE for molecular resonance identification, paired with the accomplishments of HTC in classical scientific computing for applications ranging from biochemical network¹²⁹ to high-energy particle physics¹³⁰ simulations, open the door to a powerful strategy of executing computational tasks in parallel yet taking advantage of asynchronicity.

Acknowledgements

The authors thank Preetham Tikkireddi for insight into Qiskit implementation, John Hawthorne for contributions to early versions of the code, and the University of Wisconsin-Madison Cen-

²Note identification of additional states with qDRIVE is expected to indirectly depend on the matrix size due to the need for successive deflations. However, this dependence may be removed via substitution of the VQD routine with a suitable alternative for high-lying eigenstate identification. Likewise, although at its face the number of terms appears to scale with the matrix size as $t \propto N^2$, the number of terms is generically reducible to the number of groups of commuting Pauli strings according to the method of commuting strings¹²³ and in many cases the number of terms is naturally significantly lower due to fortuitous construction of the Hamiltonian.

ter for High-Throughput Computing and HTCCondor Team for support with high-throughput computing implementation. Support for this research was provided by the Office of the Vice Chancellor for Research and Graduate Education at the University of Wisconsin-Madison with funding from the Wisconsin Alumni Research Foundation and with quantum computing resources from IBM Quantum and the Chicago Quantum Exchange.

References

- (1) Abrams, D. S.; Lloyd, S. Quantum algorithm providing exponential speed increase for finding eigenvalues and eigenvectors. *Physical Review Letters* **1999**, *83*, 5162.
- (2) Farhi, E.; Goldstone, J.; Gutmann, S.; Sipser, M. Quantum computation by adiabatic evolution. *arXiv preprint quant-ph/0001106* **2000**,
- (3) Peruzzo, A.; McClean, J.; Shadbolt, P.; Yung, M.-H.; Zhou, X.-Q.; Love, P. J.; Aspuru-Guzik, A.; O'Brien, J. L. A variational eigenvalue solver on a photonic quantum processor. *Nature Communications* **2014**, *5*, 4213.
- (4) Albash, T.; Lidar, D. A. Adiabatic quantum computation. *Reviews of Modern Physics* **2018**, *90*, 015002.
- (5) Motta, M.; Sun, C.; Tan, A. T.; O'Rourke, M. J.; Ye, E.; Minnich, A. J.; Brandao, F. G.; Chan, G. K.-L. Determining eigenstates and thermal states on a quantum computer using quantum imaginary time evolution. *Nature Physics* **2020**, *16*, 205–210.
- (6) Kyaw, T. H.; Soley, M. B.; Allen, B.; Bergold, P.; Sun, C.; Batista, V. S.; Aspuru-Guzik, A. Boosting quantum amplitude exponentially in variational quantum algorithms. *Quantum Science and Technology* **2023**, *9*, 01LT01.
- (7) Hejazi, K.; Motta, M.; Chan, G. K.-L. Adiabatic quantum imaginary time evolution. *Physical Review Research* **2024**, *6*, 033084.

- (8) Santagati, R.; Wang, J.; Gentile, A. A.; Paesani, S.; Wiebe, N.; McClean, J. R.; Morley-Short, S.; Shadbolt, P. J.; Bonneau, D.; Silverstone, J. W.; Tew, D. P.; Zhou, X.; O'Brien, J. L.; Thompson, M. G. Witnessing eigenstates for quantum simulation of Hamiltonian spectra. *Science Advances* **2018**, *4*, eaap9646.
- (9) Colless, J. I.; Ramasesh, V. V.; Dahlen, D.; Blok, M. S.; Kimchi-Schwartz, M. E.; McClean, J. R.; Carter, J.; de Jong, W. A.; Siddiqi, I. Computation of molecular spectra on a quantum processor with an error-resilient algorithm. *Physical Review X* **2018**, *8*, 011021.
- (10) Higgott, O.; Wang, D.; Brierley, S. Variational quantum computation of excited states. *Quantum* **2019**, *3*, 156.
- (11) Nakanishi, K. M.; Mitarai, K.; Fujii, K. Subspace-search variational quantum eigensolver for excited states. *Physical Review Research* **2019**, *1*, 033062.
- (12) Ollitrault, P. J.; Kandala, A.; Chen, C.-F.; Barkoutsos, P. K.; Mezzacapo, A.; Pistoi, M.; Sheldon, S.; Woerner, S.; Gambetta, J. M.; Tavernelli, I. Quantum equation of motion for computing molecular excitation energies on a noisy quantum processor. *Physical Review Research* **2020**, *2*, 043140.
- (13) Kuroiwa, K.; Nakagawa, Y. O. Penalty methods for a variational quantum eigensolver. *Physical Review Research* **2021**, *3*, 013197.
- (14) Kim, Y.; Krylov, A. I. Two algorithms for excited-state quantum solvers: Theory and application to EOM-UCCSD. *Journal of Physical Chemistry A* **2023**, *127*, 6552–6566.
- (15) Wang, Y.; Mazziotti, D. A. Electronic excited states from a variance-based contracted quantum eigensolver. *Physical Review A* **2023**, *108*, 022814.
- (16) Cianci, C.; Santos, L. F.; Batista, V. S. Subspace-Search Quantum Imaginary Time

- Evolution for Excited State Computations. *Journal of Chemical Theory and Computation* **2024**, *20*, 8940–8947.
- (17) Grimsley, H. R.; Evangelista, F. A. Challenging excited states from adaptive quantum eigensolvers: subspace expansions vs. state-averaged strategies. *Quantum Science and Technology* **2025**, *10*, 025003.
- (18) Delgado-Granados, L. H.; Krogmeier, T. J.; Sager-Smith, L. M.; Avdic, I.; Hu, Z.; Sajjan, M.; Abbasi, M.; Smart, S. E.; Narang, P.; Kais, S.; Schlimgen, A. W.; Head-Marsden, K.; Mazziotti, D. A. Quantum algorithms and applications for open quantum systems. *Chemical Reviews* **2025**, *125*, 1823–1839.
- (19) Wasielewski, M. R. et al. Exploiting chemistry and molecular systems for quantum information science. *Nature Reviews Chemistry* **2020**, *4*, 490–504.
- (20) Wang, H.; Wu, L.-A.; Liu, Y.-x.; Nori, F. Measurement-based quantum phase estimation algorithm for finding eigenvalues of non-unitary matrices. *Physical Review A* **2010**, *82*, 062303.
- (21) Daskin, A.; Grama, A.; Kais, S. A universal quantum circuit scheme for finding complex eigenvalues. *Quantum Information Processing* **2014**, *13*, 333–353.
- (22) Parker, J. B.; Joseph, I. Quantum phase estimation for a class of generalized eigenvalue problems. *Physical Review A* **2020**, *102*, 022422.
- (23) Shao, C.; Liu, J.-P. Quantum algorithms for the polynomial eigenvalue problems. *arXiv preprint arXiv:2010.15027* **2020**,
- (24) Teplukhin, A.; Kendrick, B. K.; Babikov, D. Solving complex eigenvalue problems on a quantum annealer with applications to quantum scattering resonances. *Physical Chemistry Chemical Physics* **2020**, *22*, 26136–26144.

- (25) Shao, C. Computing eigenvalues of diagonalizable matrices on a quantum computer. *ACM Transactions on Quantum Computing* **2022**, *3*, 1–20.
- (26) Zhao, H.; Zhang, P.; Wei, T.-C. A universal variational quantum eigensolver for non-Hermitian systems. *Scientific Reports* **2023**, *13*, 22313.
- (27) Singh, A.; Maheshwar, R.; Siwach, P.; Singh, N.; Arumugam, P. Quantum Simulation of Complex-Scaled Hamiltonian. *Department of Atomic Energy Symposium on Nuclear Physics* **2024**, *67*, 209–210.
- (28) Xie, X.-D.; Xue, Z.-Y.; Zhang, D.-B. Variational quantum algorithms for scanning the complex spectrum of non-Hermitian systems. *Frontiers of Physics* **2024**, *19*, 41202.
- (29) Hancock, J.; Craven, M. J.; McNeile, C.; Vadamchinn, D. Quantum Phase Transition of Non-Hermitian Systems using Variational Quantum Techniques. *arXiv preprint arXiv:2501.17003* **2025**,
- (30) Singh, A.; Siwach, P.; Arumugam, P. Quantum simulations of nuclear resonances with variational methods. *Physical Review C* **2025**, *112*, 024323.
- (31) Park, J. J.; Lu, Y.-K.; Jamison, A. O.; Tscherbil, T. V.; Ketterle, W. A Feshbach resonance in collisions between triplet ground-state molecules. *Nature* **2023**, *614*, 54–58.
- (32) Jagau, T.-C.; Bravaya, K. B.; Krylov, A. I. Extending Quantum Chemistry of Bound States to Electronic Resonances. *Annual Review of Physical Chemistry* **2017**, *68*, 525–553.
- (33) Cornish, S. L.; Tarbutt, M. R.; Hazzard, K. R. Quantum computation and quantum simulation with ultracold molecules. *Nature Physics* **2024**, *20*, 730–740.
- (34) Son, H.; Park, J. J.; Lu, Y.-K.; Jamison, A. O.; Karman, T.; Ketterle, W. Control of reactive collisions by quantum interference. *Science* **2022**, *375*, 1006–1010.

- (35) Kosloff, R.; Cerjan, C. Dynamical atom/surface effects: Quantum mechanical scattering and desorption. *Journal of Chemical Physics* **1984**, *81*, 3722–3729.
- (36) Jolicard, G.; Austin, E. J. Optical potential stabilisation method for predicting resonance levels. *Chemical Physics Letters* **1985**, *121*, 106–110.
- (37) Kosloff, R.; Kosloff, D. Absorbing boundaries for wave propagation problems. *Journal of Computational Physics* **1986**, *63*, 363–376.
- (38) Neuhasuer, D.; Baer, M. The time-dependent Schrödinger equation: Application of absorbing boundary conditions. *Journal of Chemical Physics* **1989**, *90*, 4351–4355.
- (39) Muga, J.; Palao, J.; Navarro, B.; Egusquiza, I. Complex absorbing potentials. *Physics Reports* **2004**, *395*, 357–426.
- (40) Aguilar, J.; Combes, J.-M. A class of analytic perturbations for one-body Schrödinger Hamiltonians. *Communications in Mathematical Physics* **1971**, *22*, 269–279.
- (41) Balslev, E.; Combes, J.-M. Spectral properties of many-body Schrödinger operators with dilatation-analytic interactions. *Communications in Mathematical Physics* **1971**, *22*, 280–294.
- (42) Livshits, M. The application of non-self-adjoint operators to scattering theory. *Soviet Physics, Journal of Experimental and Theoretical Physics* **1957**, *4*, 91–98.
- (43) Feshbach, H. Unified theory of nuclear reactions. *Annals of Physics* **1958**, *5*, 357–390.
- (44) Feshbach, H. A unified theory of nuclear reactions. II. *Annals of Physics* **1962**, *19*, 287–313.
- (45) Taylor, H. S.; Nazarov, G. V.; Golebiewski, A. Qualitative aspects of resonances in electron–atom and electron–molecule scattering, excitation, and reactions. *Journal of Chemical Physics* **1966**, *45*, 2872–2888.

- (46) Eliezer, I.; Taylor, H.; Williams, J. K. Resonant states of H_2^- . *Journal of Chemical Physics* **1967**, *47*, 2165–2177.
- (47) Taylor, H. S. Models, Interpretations, and Calculations Concerning Resonant Electron Scattering Processes in Atoms and Molecules. *Advances in Chemical Physics*. 1970; pp 91–147.
- (48) Kukulin, V.; Krasnopol'sky, V. Description of few-body systems via analytical continuation in coupling constant. *Journal of Physics A: Mathematical and General* **1977**, *10*, L33.
- (49) Kukulin, V.; Krasnopol'skii, V.; Miselkhi, M. Method of analytic continuation in the coupling constant in the theory of systems of several particles. Resonance state as analytic continuation of a bound state. *Soviet Journal of Nuclear Physics (English Translation)* **1979**, *29*.
- (50) Descouvemont, P.; Dohet-Eraly, J. Resonances in the R-matrix method. *Few-Body Systems* **2024**, *65*, 9.
- (51) Yarkoni, S.; Raponi, E.; Bäck, T.; Schmitt, S. Quantum annealing for industry applications: Introduction and review. *Reports on Progress in Physics* **2022**, *85*, 104001.
- (52) Zhang, H.; Bai, D.; Ren, Z. Iterative Harrow-Hassidim-Lloyd quantum algorithm for solving resonances with eigenvector continuation. *arXiv preprint arXiv:2506.20929* **2025**,
- (53) Bian, T.; Murphy, D.; Xia, R.; Daskin, A.; Kais, S. Quantum computing methods for electronic states of the water molecule. *Molecular Physics* **2019**, *117*, 2069–2082.
- (54) Zhang, H.; Bai, D.; Ren, Z. Quantum computing for extracting nuclear resonances. *Physics Letters B* **2025**, *860*, 139187.

- (55) Cao, Y.; Romero, J.; Olson, J. P.; Degroote, M.; Johnson, P. D.; Kieferová, M.; Kivlichan, I. D.; Menke, T.; Peropadre, B.; Sawaya, N. P.; Sim, S.; Veis, L.; Aspuru-Guzik, A. Quantum chemistry in the age of quantum computing. *Chemical Reviews* **2019**, *119*, 10856–10915.
- (56) McArdle, S.; Endo, S.; Aspuru-Guzik, A.; Benjamin, S. C.; Yuan, X. Quantum computational chemistry. *Reviews of Modern Physics* **2020**, *92*, 015003.
- (57) Cerezo, M.; Arrasmith, A.; Babbush, R.; Benjamin, S. C.; Endo, S.; Fujii, K.; McClean, J. R.; Mitarai, K.; Yuan, X.; Cincio, L.; Coles, P. J. Variational quantum algorithms. *Nature Reviews Physics* **2021**, *3*, 625–644.
- (58) Tilly, J.; Chen, H.; Cao, S.; Picozzi, D.; Setia, K.; Li, Y.; Grant, E.; Wossnig, L.; Rungger, I.; Booth, G. H.; Tennyson, J. The Variational Quantum Eigensolver: A review of methods and best practices. *Physics Reports* **2022**, *986*, 1–128.
- (59) Leforestier, C.; Wyatt, R. E. Optical potential for laser induced dissociation. *Journal of Chemical Physics* **1983**, *78*, 2334–2344.
- (60) Leforestier, C.; Wyatt, R. E. Role of Feshbach resonances in the infrared multiphoton dissociation of small molecules. *Journal of Chemical Physics* **1985**, *82*, 752–757.
- (61) Herzenberg, A.; Mandl, F. Resonant electron scattering by atoms. *Proceedings of the Royal Society A* **1963**, *274*, 253–266.
- (62) Moiseyev, N.; Certain, P.; Weinhold, F. Resonance Properties of Complex-Rotated Hamiltonians. *Molecular Physics* **1978**, *36*, 1613–1630.
- (63) Konotop, V. V.; Yang, J.; Zezyulin, D. A. Nonlinear waves in PT-symmetric systems. *Reviews of Modern Physics* **2016**, *88*, 035002.
- (64) Miri, M.-A.; Alu, A. Exceptional points in optics and photonics. *Science* **2019**, *363*, eaar7709.

- (65) Özdemir, Ş. K.; Rotter, S.; Nori, F.; Yang, L. Parity–time symmetry and exceptional points in photonics. *Nature Materials* **2019**, *18*, 783–798.
- (66) Moiseyev, N.; Friedland, S. Association of resonance states with the incomplete spectrum of finite complex-scaled Hamiltonian matrices. *Physical Review A* **1980**, *22*, 618.
- (67) Nimrod, M. *Non-Hermitian Quantum Mechanics*; Cambridge University Press, 2011.
- (68) Barral, D.; Cardama, F. J.; Diaz-Camacho, G.; Faílde, D.; Llovo, I. F.; Mussa-Juane, M.; Vázquez-Pérez, J.; Villasuso, J.; Piñeiro, C.; Costas, N.; Pichel, J. C.; Pena, T. F.; Gómez, A. Review of distributed quantum computing: from single QPU to high performance quantum computing. *Computer Science Review* **2025**, *57*, 100747.
- (69) Elsharkawy, A.; To, X.-T. M.; Seitz, P.; Chen, Y.; Stade, Y.; Geiger, M.; Huang, Q.; Guo, X.; Ansari, M. A.; Mendl, C. B.; Kranzlmüller, D.; Schulz, M. Integration of quantum accelerators with high performance computing—a review of quantum programming tools. *ACM Transactions on Quantum Computing* **2025**, *6*, 1–46.
- (70) Rallis, K.; Liliopoulos, I.; Varsamis, G. D.; Tsipas, E.; Karafyllidis, I. G.; Sirakoulis, G. C.; Dimitrakis, P. Interfacing Quantum Computing Systems with High-Performance Computing Systems: An Overview. *arXiv preprint arXiv:2509.06205* **2025**,
- (71) Mansfield, E.; Seegerer, S.; Vesanen, P.; Echavarria, J.; Mete, B.; Farooqi, M. N.; Schulz, L. First Practical Experiences Integrating Quantum Computers with HPC Resources: A Case Study With a 20-qubit Superconducting Quantum Computer. *arXiv preprint arXiv:2509.12949* **2025**,
- (72) Litzkow, M. J. Remote Unix: Turning idle workstations into cycle servers. Proceedings of the Summer USENIX Conference. 1987; pp 381–384.

- (73) Litzkow, M.; Livny, M.; Mutka, M. Condor—a hunter of idle workstations. The 8th International Conference on Distributed Computing Systems. 1988; pp 104–111.
- (74) Livny, M.; Basney, J.; Raman, R.; Tannenbaum, T. Mechanisms for high throughput computing. *SPEEDUP journal* **1997**, *11*, 36–40.
- (75) Basney, J. Deploying a high throughput computing cluster. *High Performance Cluster Computing* **1999**, *1*.
- (76) Thain, D.; Tannenbaum, T.; Livny, M. Distributed computing in practice: the Condor experience. *Concurrency and Computation: Practice and Experience* **2005**, *17*, 323–356.
- (77) Morgan, M.; Grimshaw, A. High-throughput computing in the sciences. *Methods in Enzymology* **2009**, *467*, 197–227.
- (78) Fajardo, E.; Dost, J.; Holzman, B.; Tannenbaum, T.; Letts, J.; Tiradani, A.; Bockelman, B.; Frey, J.; Mason, D. How much higher can HTCondor fly? Journal of Physics: Conference Series. 2015; p 062014.
- (79) Grid, O. S. Intermediate DAGMan. <https://github.com/OSGConnect/tutorial-dagman-intermediate>, 2024.
- (80) Isakov, S. V. et al. Simulations of quantum circuits with approximate noise using qsim and Cirq. *arXiv preprint arXiv:2111.02396* **2021**,
- (81) Pordes, R. et al. The open science grid. Journal of Physics: Conference Series. 2007.
- (82) Altunay, M. et al. A science driven production cyberinfrastructure—the open science grid. *Journal of Grid Computing* **2011**, *9*, 201–218.
- (83) Endo, S.; Benjamin, S. C.; Li, Y. Practical quantum error mitigation for near-future applications. *Physical Review X* **2018**, *8*, 031027.

- (84) Cai, Z.; Babbush, R.; Benjamin, S. C.; Endo, S.; Huggins, W. J.; Li, Y.; McClean, J. R.; O’Brien, T. E. Quantum error mitigation. *Reviews of Modern Physics* **2023**, *95*, 045005.
- (85) Dewes, A.; Ong, F. R.; Schmitt, V.; Lauro, R.; Boulant, N.; Bertet, P.; Vion, D.; Esteve, D. Characterization of a two-transmon processor with individual single-shot qubit readout. *Physical Review Letters* **2012**, *108*, 057002.
- (86) Maciejewski, F. B.; Zimborás, Z.; Oszmaniec, M. Mitigation of readout noise in near-term quantum devices by classical post-processing based on detector tomography. *Quantum* **2020**, *4*, 257.
- (87) Geller, M. R. Rigorous measurement error correction. *Quantum Science and Technology* **2020**, *5*, 03LT01.
- (88) Temme, K.; Bravyi, S.; Gambetta, J. M. Error mitigation for short-depth quantum circuits. *Physical Review Letters* **2017**, *119*, 180509.
- (89) Kandala, A.; Temme, K.; Córcoles, A. D.; Mezzacapo, A.; Chow, J. M.; Gambetta, J. M. Error mitigation extends the computational reach of a noisy quantum processor. *Nature* **2019**, *567*, 491–495.
- (90) Giurgica-Tiron, T.; Hindy, Y.; LaRose, R.; Mari, A.; Zeng, W. J. Digital zero noise extrapolation for quantum error mitigation. 2020 IEEE International Conference on Quantum Computing and Engineering. 2020; pp 306–316.
- (91) Miller, A. X.; Soley, M. B. Universal Quantum Error Mitigation via Random Inverse Depolarizing Approximation. *arXiv preprint arXiv:2508.17513* **2025**,
- (92) Riss, U. V.; Meyer, H. D. Calculation of resonance energies and widths using the complex absorbing potential method. *Journal of Physics B* **1993**, *26*, 4503.

- (93) Zhang, D.-B.; Chen, B.-L.; Yuan, Z.-H.; Yin, T. Variational quantum eigensolvers by variance minimization. *Chinese Physics B* **2022**, *31*, 120301.
- (94) Warren, S.; Wang, Y.; Benavides-Riveros, C. L.; Mazziotti, D. A. Exact ansatz of fermion-boson systems for a quantum device. *Physical Review Letters* **2024**, *133*, 080202.
- (95) Zhang, F.; Gomes, N.; Yao, Y.; Orth, P. P.; Iadecola, T. Adaptive variational quantum eigensolvers for highly excited states. *Physical Review B* **2021**, *104*, 075159.
- (96) Boyd, G.; Koczor, B. Training variational quantum circuits with CoVaR: Covariance root finding with classical shadows. *Physical Review X* **2022**, *12*, 041022.
- (97) Hobday, I.; Stevenson, P.; Benstead, J. Variance minimisation on a quantum computer for nuclear structure. *arXiv preprint arXiv:2209.07820* **2022**,
- (98) Liu, S.; Zhang, S.-X.; Hsieh, C.-Y.; Zhang, S.; Yao, H. Probing many-body localization by excited-state variational quantum eigensolver. *Physical Review B* **2023**, *107*, 024204.
- (99) Buhrman, H.; Cleve, R.; Watrous, J.; De Wolf, R. Quantum fingerprinting. *Physical Review Letters* **2001**, *87*, 167902.
- (100) Gottesman, D.; Chuang, I. Quantum digital signatures. *arXiv preprint quant-ph/0105032* **2001**,
- (101) Garcia-Escartin, J. C.; Chamorro-Posada, P. SWAP test and Hong-Ou-Mandel effect are equivalent. *Physical Review A* **2013**, *87*, 052330.
- (102) Cincio, L.; Subaşı, Y.; Sornborger, A. T.; Coles, P. J. Learning the quantum algorithm for state overlap. *New Journal of Physics* **2018**, *20*, 113022.

- (103) Havlíček, V.; Córcoles, A. D.; Temme, K.; Harrow, A. W.; Kandala, A.; Chow, J. M.; Gambetta, J. M. Supervised learning with quantum-enhanced feature spaces. *Nature* **2019**, *567*, 209–212.
- (104) Powell, M. J. A direct search optimization method that models the objective and constraint functions by linear interpolation. *Advances in optimization and numerical analysis*. 1994; pp 51–67.
- (105) Nakanishi, K. M.; Fujii, K.; Todo, S. Sequential minimal optimization for quantum-classical hybrid algorithms. *Physical Review Research* **2020**, *2*.
- (106) Powell, M. J. The BOBYQA algorithm for bound constrained optimization without derivatives. *Cambridge NA Report NA2009/06, University of Cambridge, Cambridge* **2009**, *26*, 26–46.
- (107) Cartis, C.; Fiala, J.; Marteau, B.; Roberts, L. Improving the flexibility and robustness of model-based derivative-free optimization solvers. *ACM Transactions on Mathematical Software (TOMS)* **2019**, *45*, 1–41.
- (108) Karalekas, P. J.; Tezak, N. A.; Peterson, E. C.; Ryan, C. A.; Da Silva, M. P.; Smith, R. S. A quantum-classical cloud platform optimized for variational hybrid algorithms. *Quantum Science and Technology* **2020**, *5*, 024003.
- (109) Van Den Berg, E.; Mineev, Z. K.; Temme, K. Model-free readout-error mitigation for quantum expectation values. *Physical Review A* **2022**, *105*, 032620.
- (110) Lorenz, J. M.; Monz, T.; Eisert, J.; Reitzner, D.; Schopfer, F.; Barbaresco, F.; Kurowski, K.; van der Schoot, W.; Strohm, T.; Senellart, J.; Perrault, C. M.; Knufinke, M.; Amodjee, Z.; Giardini, M. Systematic benchmarking of quantum computers: status and recommendations. *arXiv preprint arXiv:2503.04905* **2025**,

- (111) Dai, J.; Vidwans, A.; Wan, E. H.; Miller, A. X.; Hawthorne, J. M.; Soley, M. B. qDRIVE. <https://github.com/ericwan808/qDRIVE>, 2026.
- (112) Javadi-Abhari, A.; Treinish, M.; Krsulich, K.; Wood, C. J.; Lishman, J.; Gacon, J.; Martiel, S.; Nation, P. D.; Bishop, L. S.; Cross, A. W.; Johnson, B. R.; Gambetta, J. M. Quantum computing with Qiskit. *arXiv preprint arXiv:2405.08810* **2024**,
- (113) Bland, M. P. et al. Millisecond lifetimes and coherence times in 2D transmon qubits. *Nature* **2025**,
- (114) Wakaura, H.; Suksmono, A. B. Tangent vector variational quantum eigensolver: A robust variational quantum eigensolver against the inaccuracy of derivative. *arXiv preprint arXiv:2105.01141* **2021**,
- (115) Kassal, I.; Whitfield, J. D.; Perdomo-Ortiz, A.; Yung, M.-H.; Aspuru-Guzik, A. Simulating chemistry using quantum computers. *Annual Review of Physical Chemistry* **2011**, *62*, 185–207.
- (116) Jagau, T.-C. Theory of electronic resonances: fundamental aspects and recent advances. *Chemical Communications* **2022**, *58*, 5205–5224.
- (117) Bauer, B.; Bravyi, S.; Motta, M.; Chan, G. K.-L. Quantum algorithms for quantum chemistry and quantum materials science. *Chemical Reviews* **2020**, *120*, 12685–12717.
- (118) Jordan, P.; Wigner, E. Über das Paulische Äquivalenzverbot. *Zeitschrift für Physik* **1928**, *47*, 631–651.
- (119) Bravyi, S. B.; Kitaev, A. Y. Fermionic quantum computation. *Annals of Physics* **2002**, *298*, 210–226.
- (120) Aaronson, S. Shadow tomography of quantum states. Proceedings of the 50th annual ACM SIGACT symposium on theory of computing. 2018; pp 325–338.

- (121) Aaronson, S.; Rothblum, G. N. Gentle measurement of quantum states and differential privacy. Proceedings of the 51st Annual ACM SIGACT Symposium on Theory of Computing. 2019; pp 322–333.
- (122) Huang, H.-Y.; Kueng, R.; Preskill, J. Predicting many properties of a quantum system from very few measurements. *Nature Physics* **2020**, *16*, 1050–1057.
- (123) McClean, J. R.; Romero, J.; Babbush, R.; Aspuru-Guzik, A. The theory of variational hybrid quantum-classical algorithms. *New Journal of Physics* **2016**, *18*, 023023.
- (124) Grimsley, H. R.; Economou, S. E.; Barnes, E.; Mayhall, N. J. An adaptive variational algorithm for exact molecular simulations on a quantum computer. *Nature Communications* **2019**, *10*, 3007.
- (125) Farrell, R. C.; Illa, M.; Ciavarella, A. N.; Savage, M. J. Scalable circuits for preparing ground states on digital quantum computers: The Schwinger model vacuum on 100 qubits. *PRX Quantum* **2024**, *5*, 020315.
- (126) Smart, S. E.; Mazziotti, D. A. Quantum solver of contracted eigenvalue equations for scalable molecular simulations on quantum computing devices. *Physical Review Letters* **2021**, *126*, 070504.
- (127) Wang, Y.; Sager-Smith, L. M.; Mazziotti, D. A. Quantum simulation of bosons with the contracted quantum eigensolver. *New Journal of Physics* **2023**, *25*, 103005.
- (128) Moiseyev, N. Quantum theory of resonances: calculating energies, widths and cross-sections by complex scaling. *Physics Reports* **1998**, *302*, 212–293.
- (129) Kent, E.; Hoops, S.; Mendes, P. Condor-COPASI: high-throughput computing for biochemical networks. *BMC Systems Biology* **2012**, *6*, 91.

- (130) Tsaregorodtsev, A.; Garonne, V.; Stokes-Rees, I. DIRAC: A scalable lightweight architecture for high throughput computing. Fifth IEEE/ACM International Workshop on Grid Computing. 2004; pp 19–25.

Appendix: Edge Cases of Exponential Zero-Noise Extrapolation

In edge cases for which exponential three-point ZNE produces a physically unrealizable zero-noise result $x_0 \notin \mathcal{R}$, linear zero-noise extrapolation is employed to mitigate gate error as follows:

Where $x_3 < x_1 < x_5$, contrary to the physical expectation that noise increases monotonically with λ , the optimal least-squares curve with

$$A = (x_1 + x_3) / 2, \quad B \rightarrow 0_{\pm}, \quad C \rightarrow \infty \quad (25)$$

remains nearly constant between x_1 and x_3 and increases steeply to meet x_5 exactly; we thus exclude x_5 as an outlier and employ the zero-noise estimate

$$x_0 = (x_1 + x_3) / 2. \quad (26)$$

Where $x_1 < x_5 < x_3$, since the optimal least-squares curve with

$$A = (x_1 + x_3) / 2, \quad B \rightarrow \pm\infty, \quad C \rightarrow -\infty \quad (27)$$

yields the physically unreasonable estimate $x_0 = \pm\infty$, and since x_5 is expected to give rise to more error than x_3 where the system is not fully depolarized; we extrapolate x_1 and x_3

to x_0 via the linear fit $x_\lambda \approx A\lambda + B$ such that the zero-noise estimate is

$$x_0 = \frac{3x_1 - x_3}{2}. \quad (28)$$

Where $x_3 \approx x_5$, in order to avoid the instability $x_0 \rightarrow \pm\infty$ as $x_3 \rightarrow x_5$, we evaluate the statistical significance between x_3 and x_5 according to a two-sample z-test at the $\alpha = 0.05$ level (for which statistical evidence corresponds to a z-score of $|z| > 1.96$). Given that measurement of the ancilla projects the qubit onto either the $|0\rangle$ or $|1\rangle$ state, the n -shot standard deviation takes the form for a binomial distribution

$$s = \sqrt{\frac{p(1-p)}{n}}, \quad (29)$$

which entails a joint standard deviation of

$$s_{\text{joint}} = \sqrt{\frac{x_3(1-x_3) + x_5(1-x_5)}{n}}$$

and associated z-score of

$$z = \frac{x_3 - x_5}{\sqrt{\frac{x_3(1-x_3) + x_5(1-x_5)}{n}}}.$$

We therefore we use the exponential fit estimate Eq. (14) if

$$\frac{|x_3 - x_5|}{\sqrt{\frac{x_3(1-x_3) + x_5(1-x_5)}{n}}} > 1.96$$

and the linear fit Eq. (28) otherwise.

Where $x_1 \approx x_5$, the estimate x_0 becomes undefined (given the existence of two equally applicable but mutually inconsistent least-squares curves Eq. (25) and Eq. (27)), such that we employ the average estimate for $x_3 < x_1 < x_5$ Eq. (25) and $x_1 < x_5 < x_3$ Eq. (27)

$$x_0 = x_1. \quad (30)$$

Where $x_1 \approx x_3 \approx x_5$, the least squares curve is

$$x_1 = x_3 = x_5 = A + B, \quad C = 0, \quad (31)$$

such that we estimate x_0 as the constant value

$$x_0 = x_1 = x_3 = x_5. \quad (32)$$